UCID- 17365

Lawrence Livermore Laboratory

A Feasibility Study and Prototype Design of a NaI Gamma-Ray Densitometer for Use in LOFT

Stefan P. Swierkowski

January 7, 1977

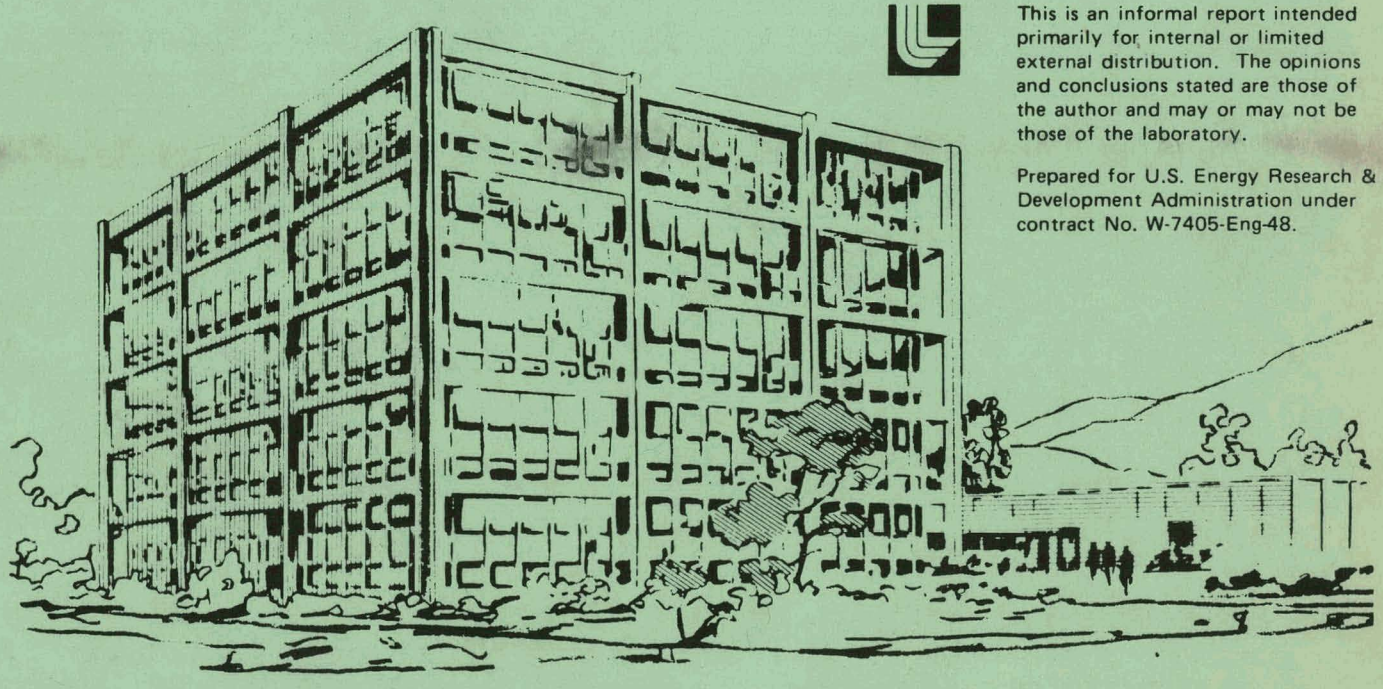

Prepared for U.S. Energy Research & Development Administration under contract No. W-7405-Eng-48.

DISCLAIMER

A Feasibility Study and Prototype Design of a NaI Gamma-Ray Densitometer for Use in LOFT

Outline

A Feasibility Study and Prototype Design of a NaI Gamma-Ray Densitometer for Use in LOFT

Introduction

This work report is part of a study for the Aerojet Nuclear Company ("A Feasibility Study for Use of a Germanium Detector in LOFT Gamma-Ray Densitometer", P.O. S-6238 11/19/75). The first report on this study (UCID-17111) indicated that NaI detectors would be preferable to germanium and all subsequent work has been confined to the use of NaI detectors. The primary aim of this study is to predict the performance of a gamma-ray densitometer system using computer modeling techniques. The system studied consists of a Co^{60} calibration source, a pipe containing a variable amount of water absorber where the water contains radioactive N^{16}, and a shielded and collimated NaI detector system. An idealized model of this system is shown in Figure 1 with the sources described in Table 1 and Figure 2. The basic question is: Can one detect the change in signal from the collimated Co^{60} calibration source caused by a water density change when the detector system is subject to an adjacent background source equivalent to about 30 Ci of high energy (avg. 6 MeV, pk. 10 MeV) gamma rays?

The first report indicated that excessive (saturation) detector count rates could easily occur from this high energy, high intensity background and the second basic question is: How much lead shielding is required for typical NaI detectors to keep the detector count rate from this source below 50 kcps (50,000 counts per second)? The importance of this question is borne out by the results that indicate that the weight of lead shielding required is about 1000 lbs.

Preliminary Considerations and Relevant Parameters

Some critical parameters in the densitometer design are the length and diameter of the detector collimator (beamed at the calibration source), the

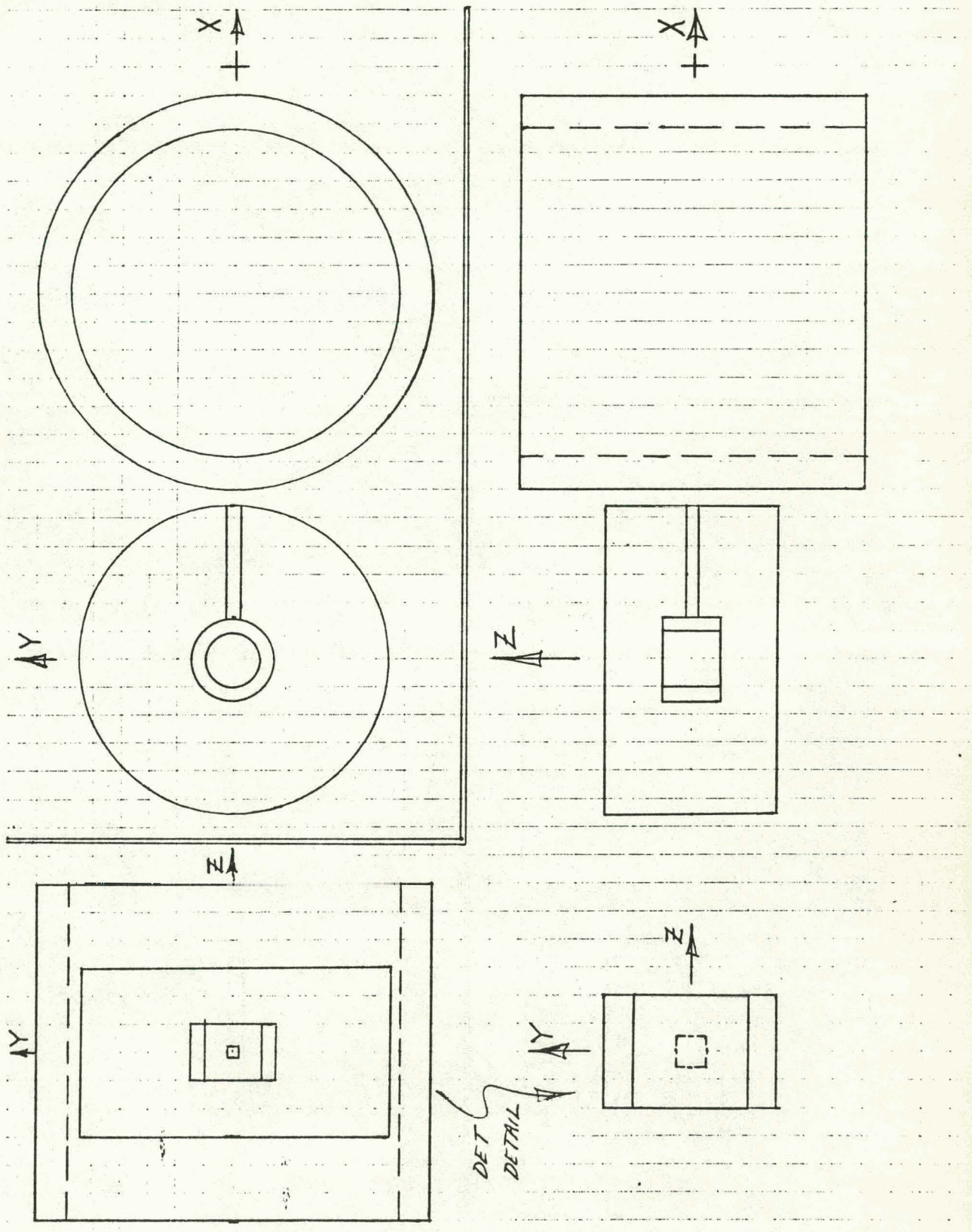

Figure 1. Densitometer geometry with a cylindrical detector shield.

TABLE 1

GAMMA RAY SOURCES FOR COMPUTER MODELING

1. 0, 10, or 50 Ci Co^{60} point source with 1332 keV and 1173 keV.

2. N^{16} 6-7 MeV, 137 $\mu Ci/cm^3$ at 75% water.

   The 6.13 MeV (69%) and 7.11 MeV (5%) emissions are modeled as one peak at 6.13 MeV (74%). Normal operation and blowdown.

3. Neutron activation gammas from shield tank 1 X 10^7 γ/cm^2-second.

   Normal operation and blowdown.

   A) Skew spectral shape of Figure 2

   or

   B) Flat spectral shape 0.5-10 MeV.

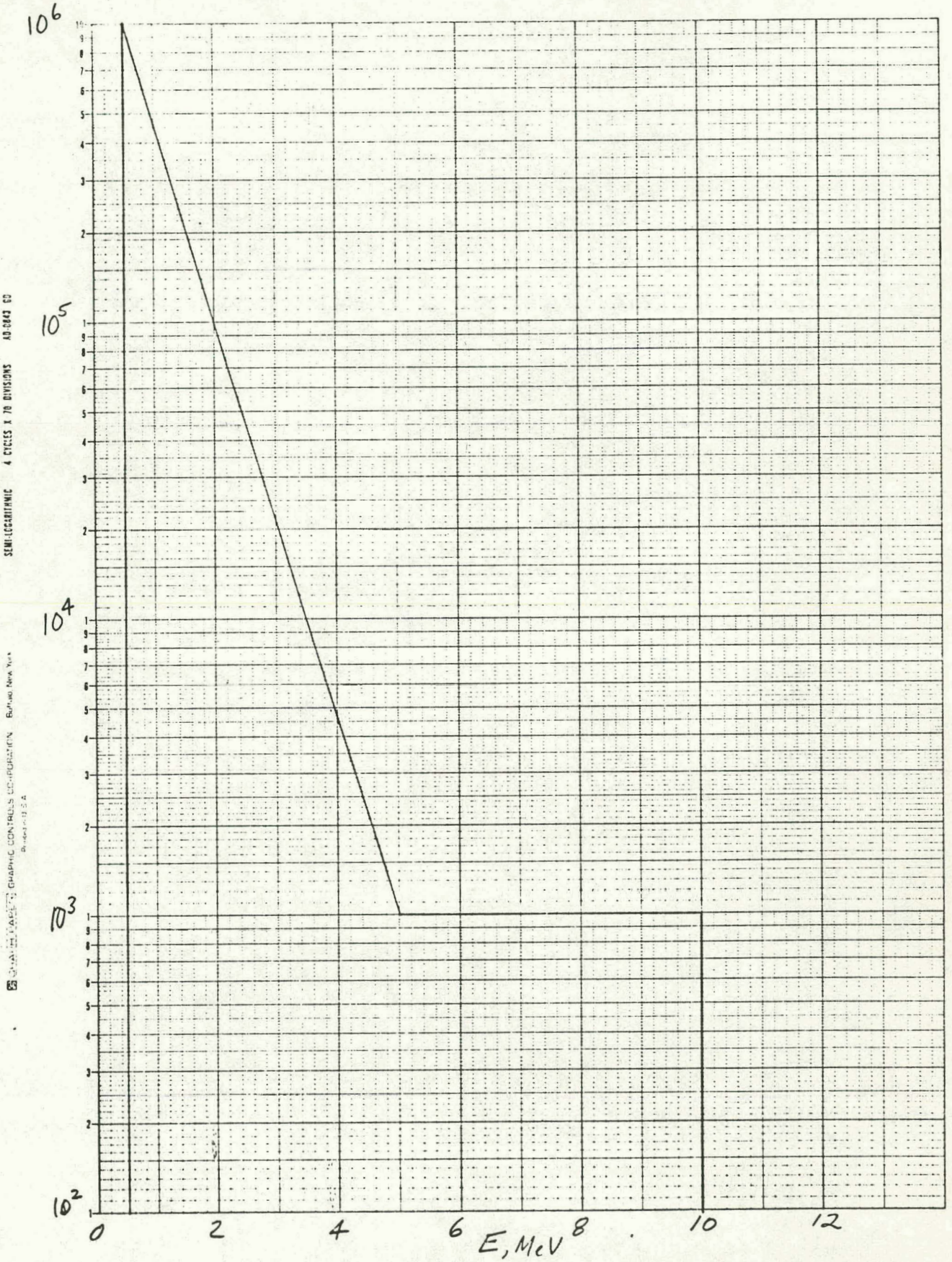

Figure 2. Skew reactor background spectrum 1 x 10^7 γ/cm^2-sec.

the calibration source energy or energies and its physical location and strength, and the detector size and location. Optimization of these and other relevant parameters involves a large number of performance tradeoff situations, many of which are coupled. For example, the calibration source to detector distance should be minimized within the constraints of desired collimator path sampling but this distance must increase as better (i.e., thicker) detector shielding is used for the high energy background reduction. Detector size also involves several tradeoffs. First, a larger detector will increase the shielding requirements rapidly because the shielding thickness must increase because the larger detector is more efficient and also the total shield diameter is increased if the detector cell diameter is increased.

The energy of the calibration source is another crucial parameter. Two key considerations are that the sensitivity of the transmitted calibration flux to the change in water density is a strong function of source energy and that the detector efficiency is a strong function of energy. The photopeak (η_p) and detection (η_D) efficiencies for some typical NaI detectors are given in Figure 3. The photopeak efficiency is the number of detector counts under the spectrum photopeak divided by the number of photons that enter the exposed detector face from a monoenergetic source; this is a strong function of source collimation and source position. The collimation parameter is specified in Figure 3 for a parallel beam of photons. The detection efficiency is all the counts in the detector spectrum divided by the number of photons that enter the exposed detector face; this is weak function of collimation and source position. The absolute efficiency for a specified source is the appropriate detector efficiency (η_p or η_D) multiplied by the fractional solid angle subtended by the appropriate exposed detector area relative to the source center. One can see from Figure 3 that the photopeak efficiency diminishes very rapidly with energy but the detection efficiency is reduced slowly. The importance of these

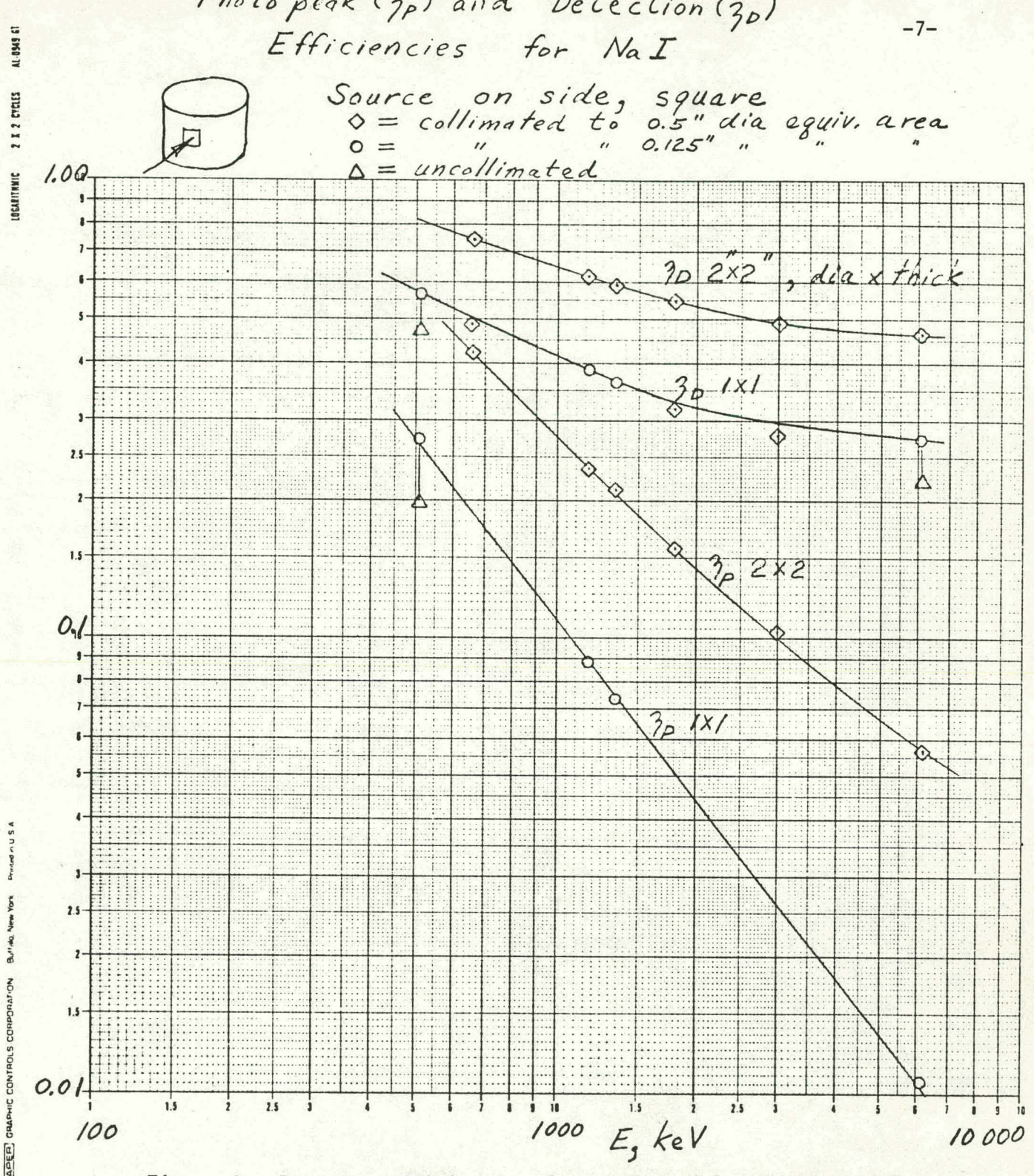

Figure 3. Detector efficiencies for various NaI detectors with several degrees of collimation for a parallel square beam of gamma rays incident on the cylindrical side.

definitions and efficiency functions bears directly on the detector size and calibration source energy that should be used. From a count rate viewpoint, when considering the reactor background and N^{16} leakage through the detector shielding, the detection efficiency (η_D) uncollimated should be used. To consider the calibration signal count rate, the photopeak efficiency (η_p) with collimation should be used.

A simple analytical calculation is now considered where one starts with a parallel collimated calibration flux incident on one side of the coolant water pipe and then into a NaI detector on the other side. If one calculates the fraction of unscattered transmitted flux (i.e., full energy photons) and multiplies this by the detector photopeak (η_p) efficiency, then the final fraction, F, may be plotted as a function of gamma ray source energy with water density as a parameter as shown in Figures 4 and 5. The difference between the curves is the sensitivity ($-dF/d\rho_{H_2O}$) to density changes in the water and is also plotted on the figures. The data in Figures 4 and 5 favor the use of a 2 x 2 (i.e., 2 in. dia. x 2 in. thick) NaI detector at about 2.4 MeV calibration source energy; the sensitivity is higher and the final fraction F, which is proportional to signal count rate, is higher. There are two problems with this choice, however. First, there is the problem of available practical sources. One ideally desires a monoenergetic source at the correct gamma energy with a high yield per decay and a half-life longer than 3-4 months. Sources with unusable emissions, especially high energy gammas and high energy bremsstrahlung, will not only require more source shielding per usable source photon but will also contribute undesired background counts in the detector spectrum. A cursory survey of commercially available sources yielded very few high intensity (1-50 Ci), high energy sources of the type desired. Sources that were considered were Cs^{137}, Co^{60}, Sb^{124}, and Tl^{208}. None of these sources are well matched for the

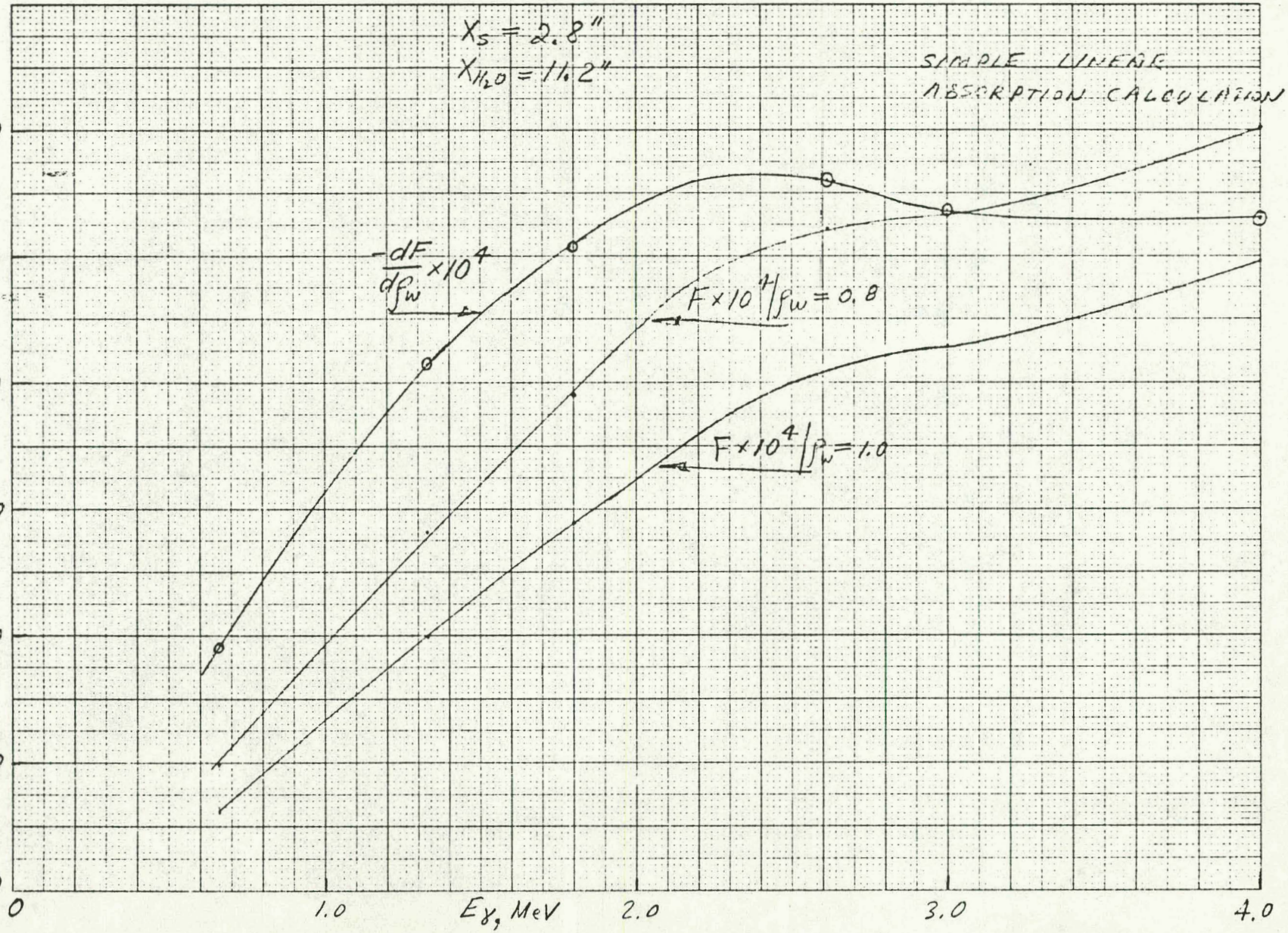

Figure 4. Photopeak fractions transmitted through pipe and absorbed in 2 x 2 NaI detector and sensitivity as a function of source energy.

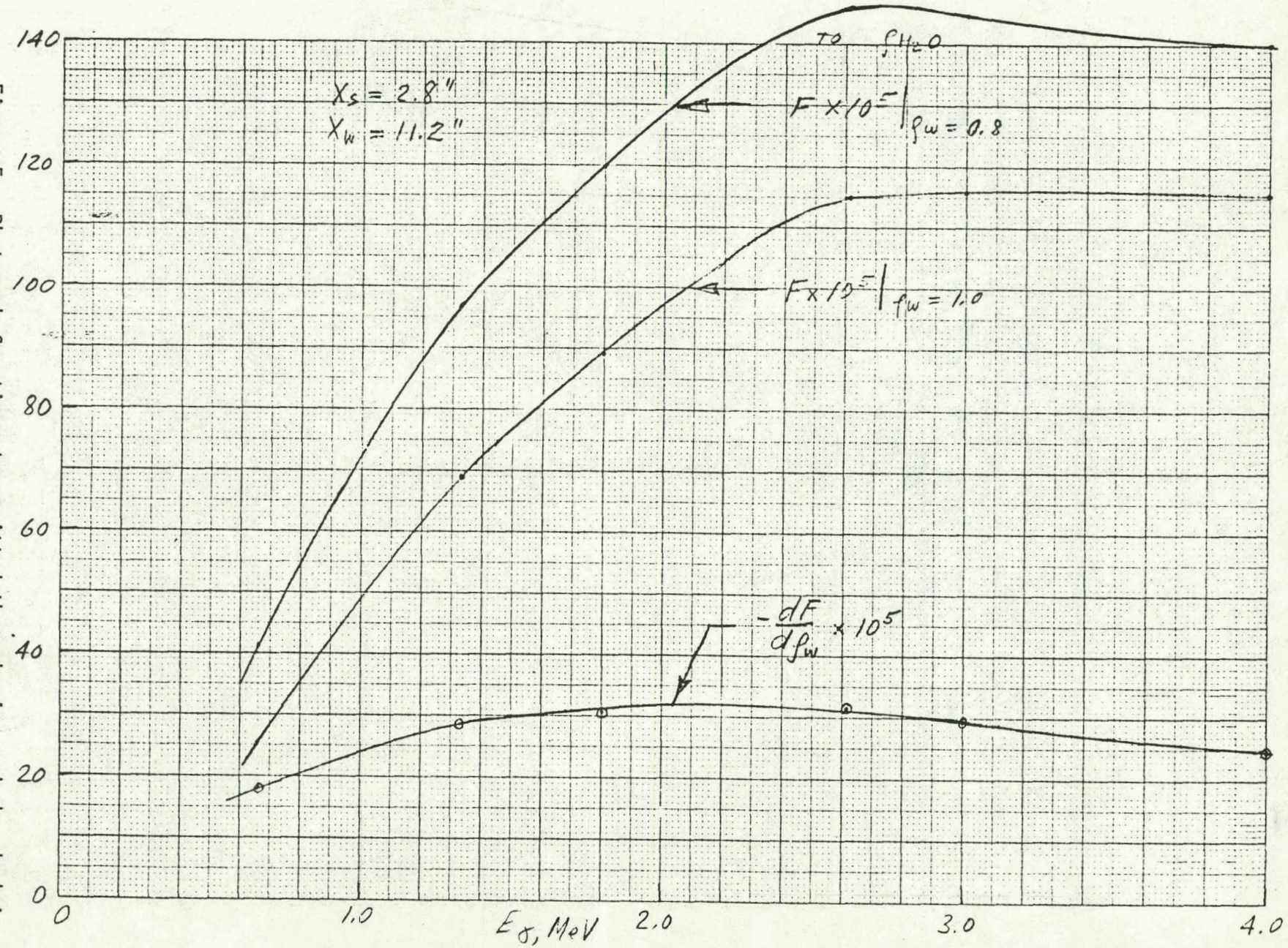

Figure 5. Photopeak fractions transmitted through pipe and absorbed in 1 x 1 NaI detector and sensitivity as a function of source energy.

2 x 2 NaI detector. For the available sources, the 2 x 2 NaI detector will perform significantly better than a 1 x 1 NaI detector, even if a non-optimum source is used. The second, and more important, problem with the 2 x 2 NaI detector size is one of detector shielding requirements from the reactor and N^{16} background. Initial calculations, to be discussed later, for a 2 x 2 NaI detector indicated the detector shielding requirements were excessive in size and weight. Since the detection efficiency of a 2 x 2 detector is about 2 times that of 1 x 1 and the area is 4 times that of a 1 x 1, for a given flux the 2 x 2 detector is about 8 times harder to shield down to a given count rate than the 1 x 1 detector. Subsequent calculations, to be discussed later, for a 1 x 1 detector showed that practical shielding dimensions and weight could be achieved. Now from Figures 4 and 5, one can see that the sensitivity versus energy curve is much flatter for the 1 x 1 detector than for the 2 x 2 detector. The optimal sensitivity energy (2.2 MeV) is still high, but the relative penalty for using a 1.33 MeV source with a 1 x 1 detector is much less than with a 2 x 2 detector.

Of the sources mentioned above, only Cs^{137} and Co^{60} are very close to ideal. The useful emissions are 662 keV (85%) for Cs^{137} and 1173 keV (100%) and 1332 keV (100%) for Co^{60}. The Co^{60} photons must be counted carefully when computing the conversion between Curies and detector count rate. There is very little angular correlation between the 1173 keV and the 1332 keV photons that are emitted with each decay; the angular distribution is uniform within $\pm$ 4.5%. For the present application where the collimated detector solid angle to the Co^{60} source is very small, if the detector detects one of the decay photons, then the probability of it also detecting the other decay photon is negligibly small. Multiple photon detector counts are not included in this modeling. From the detector standpoint, two adjacent peaks are almost as good

as one for use as a signal and in this application Co^{60} is better than Cs^{137} in sensitivity and absolute count rate. Co^{60} is spectrally much cleaner than the other sources and also much more efficient, thus it was chosen for subsequent calculations.

The Compton absorption process tends to dominate in most materials used in this study over the high energy range of approximately 1-6 MeV. From a detector viewpoint, when considering a monoenergetic source, the scattered Compton photon may escape or it may be fully absorbed or it may be scattered again. The Compton electron will deposite energy from zero up to a maximum, E_{CM}, given in Figure 6. If the Compton photon escapes, then a count in the Compton continuum is observed. If the Compton photon is fully absorbed, then a count in the photopeak is observed. Thus, from these processes the spectrum develops a shape that typically has a continuum from zero to E_{CM}, a valley between E_{CM} and $E\gamma$, and a photopeak at $E\gamma$. But there is an additional process that dominates at the highest energies and which has an energy threshold of $2\ m_o c^2 = 2 \times 511$ keV; this pair production effect is usually not significant until ~ 2 MeV. The pair production absorption creates an electron and a positron from 1022 keV of the incoming energy and transfers the balance of the energy to the electron and positron kinetic energy. When the positron's kinetic energy is transferred to the detector, it annihilates, creating two 511 keV annihilation photons. If both annihilation photons are absorbed in the detector, a count in the full energy photopeak is possible. If one (or two) of the annihilation photons escape the detector, then a count in the single (or double) escape peak is possible. For a 1 X 1 NaI detector, the electron and positron mean free paths are very small compared to the detector size; however the annihilation photon mean free paths are comparable to the detector size. For the 1 X 1 NaI detector and 6130 keV gamma rays, the double escape peak at 5108 keV has a relative

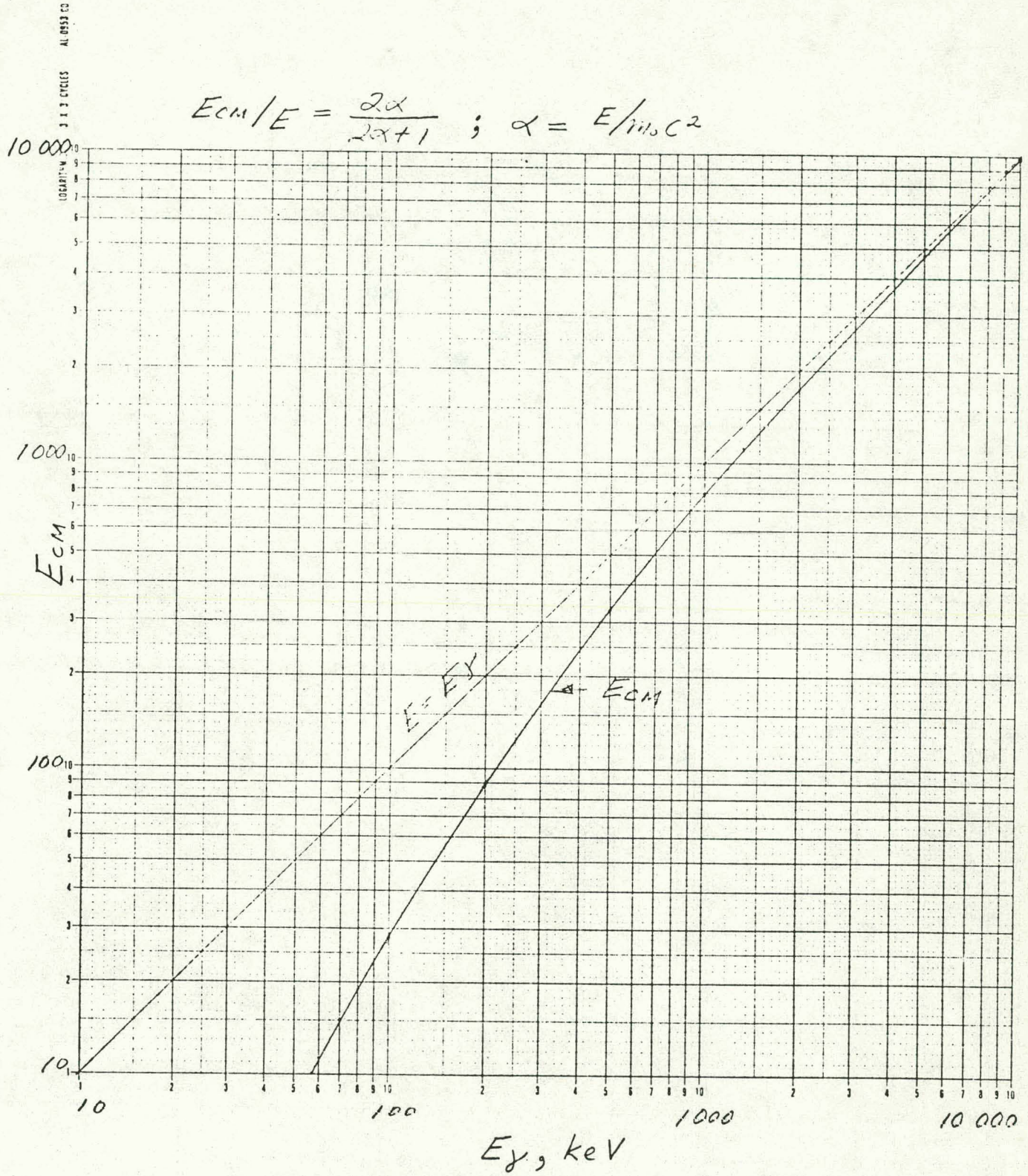

Figure 6. Maximum Compton electron energy as a function of primary photon energy.

amplitude of 7.1, the single escape peak at 5619 keV has a relative amplitude of 2.6, and the photopeak at 6130 keV has a relative amplitude of 1.0; furthermore, 80% of the detector counts are in the continuum and only 22.2% of the incoming 6130 keV gamma rays are detected at all! The full absorption photoelectric effect dominates at low energies of course. There are several other less important effects such as fluorescent x-ray escape, but the major effects described above indicate the nature of the absorbed energy spectrum in the detector. Detector and electronics noise will smear out the very narrow peaks of the absorbed energy spectrum. This noise is a complicated function of energy; some theories show it has an $E^{-1/2}$ dependence. When typical commercial data are used, the resolution (FWHM = full width at half maximum) appears to have an $E^{-1/4}$ dependence; this dependence is used in the detector simulation. The specified FWHM resolution at 662 keV is used as a reference point. If the photopeak is to be clearly resolved from the continuum, then the resolution should be less than the gap between the Compton edge and the photopeak. This is shown in Figure 7 for three typical grades of detector resolution.

Geometry Used in Computer Modeling

Two major geometries were used in the densitometer computer modeling. The first model is shown in Figure 1 (page 3) which is characterized by a cylindrical shield around a cylindrical NaI detector. The cylindrical shell shield has cylindrical end plugs and uses a square cross section collimator path. The square cross section was used because the code used (HANDYL7X - a version of SANDYL) does not allow perpendicular cylindrical geometries; the square cross section area was chosen to be equal to the area of 1/8 and 3/16 inch diameter circles. The approximation of a circular collimator by a square one should have no significant effect in the modeling. The collimator was filled with

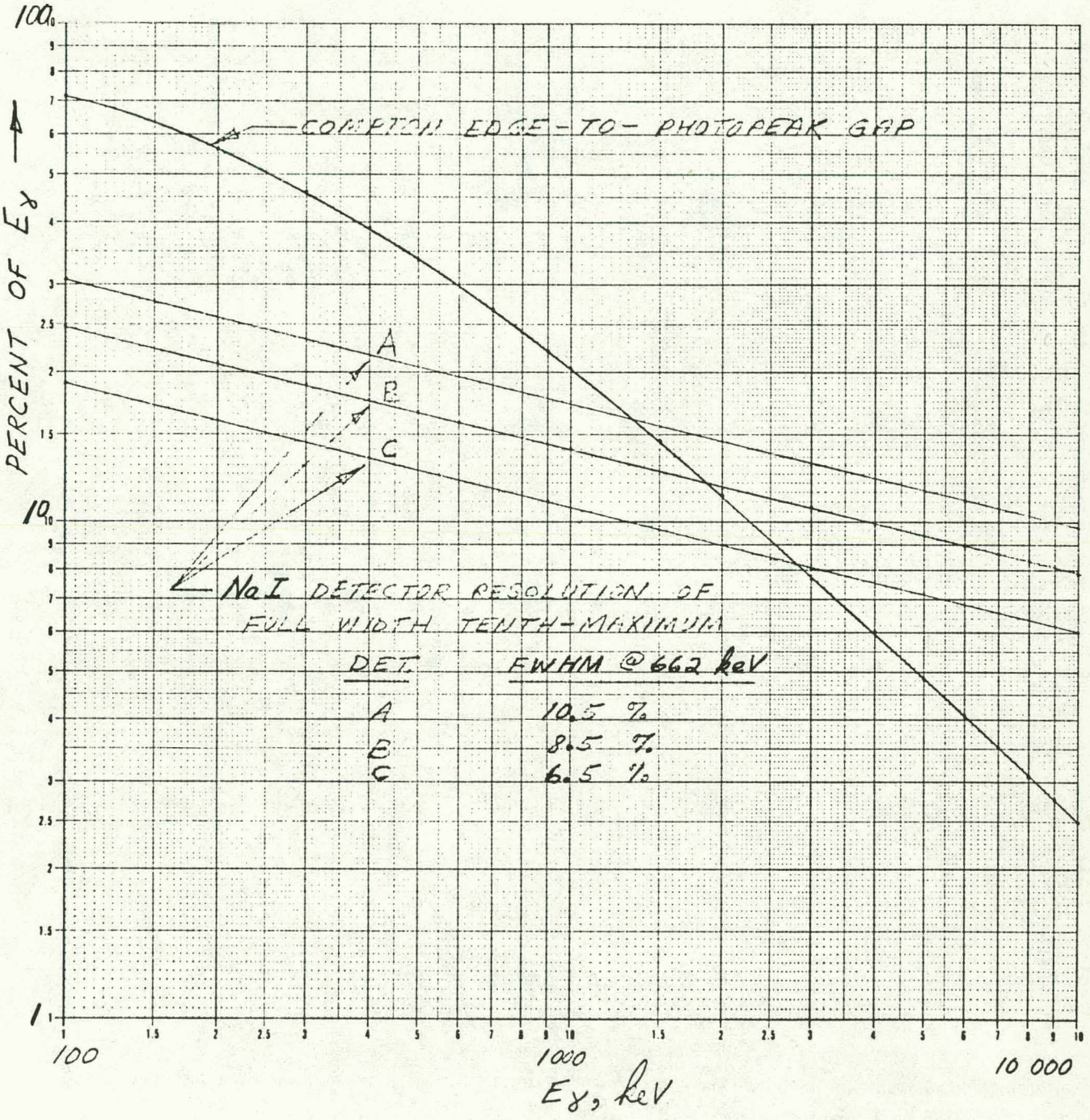
COMPTON EDGE-TO-PHOTOPEAK GRP
A
B
C
NaI DETECTOR RESOLUTION OF FULL WIDTH TENTH-MAXIMUM
DET. FWHM @662 keV
A 10.5 %
B 8.5 %
C 6.5 %
PERCENT OF Eγ
Eγ, keV
100
1000
10 000

Figure 7.

boron nitride at 1/10 bulk density. This density x path-length product for this material was chosen to minimize the attenuation of the gamma rays down the collimator to less than 20% while maximizing the absorption of the thermal neutrons; for a path length of 7 inches with 1/10 bulk density natural BN the thermal neutron transmission is 4.73×10^{-30}. The same effects could be obtained with the collimator filled with 0.7 inches of full density (2.0 gm/cc) BN and 6.3 inches filled with air or low density foam, but this combination is more cumbersome to model. The computer zoning for the cylindrical detector shield assembly of figure is shown in Figure 8. The cylindrical shield model of Figures 1 and 8 was computationally effective for computing the C_o^{60} and N^{16} transmission through the water pipe and down the collimator and near-collimator regions; but this model was very inefficient for computing the N^{16} and reactor background contribution to the detector that leaks through the thicker part of the shielding. This latter contribution is computed more efficiently and more accurately with the spherical shell shield geometry of Figure 9; this figure is approximately to scale except the pipe length is shown shortened. A spherical detector is used with a volume equal to that for 1-inch diameter by 1-inch thick NaI detector. This model is used to compute the flux spectrum entering the detector and is a good approximation to the exact geometry. Once the various flux contributions entering the detector have been computed, the flux absorbed in the detector was always computed with the true cylindrical detector shape.

The results of various geometry computations have been combined into a prototype densitometer design. The final effective model for this prototype design is shown approximately to scale in Figure 10.

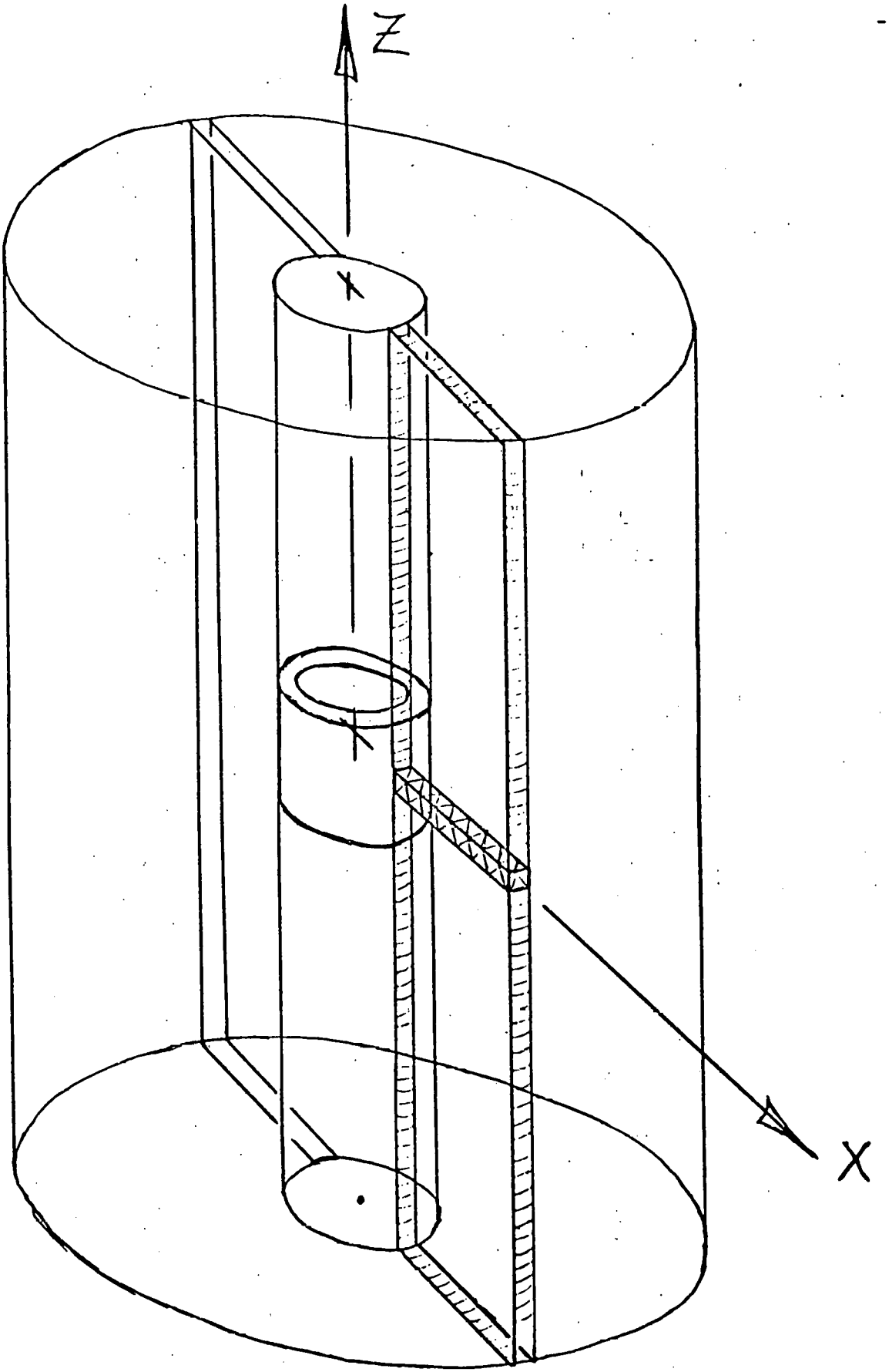

Figure 8. Cylindrical detector shield assembly model details.

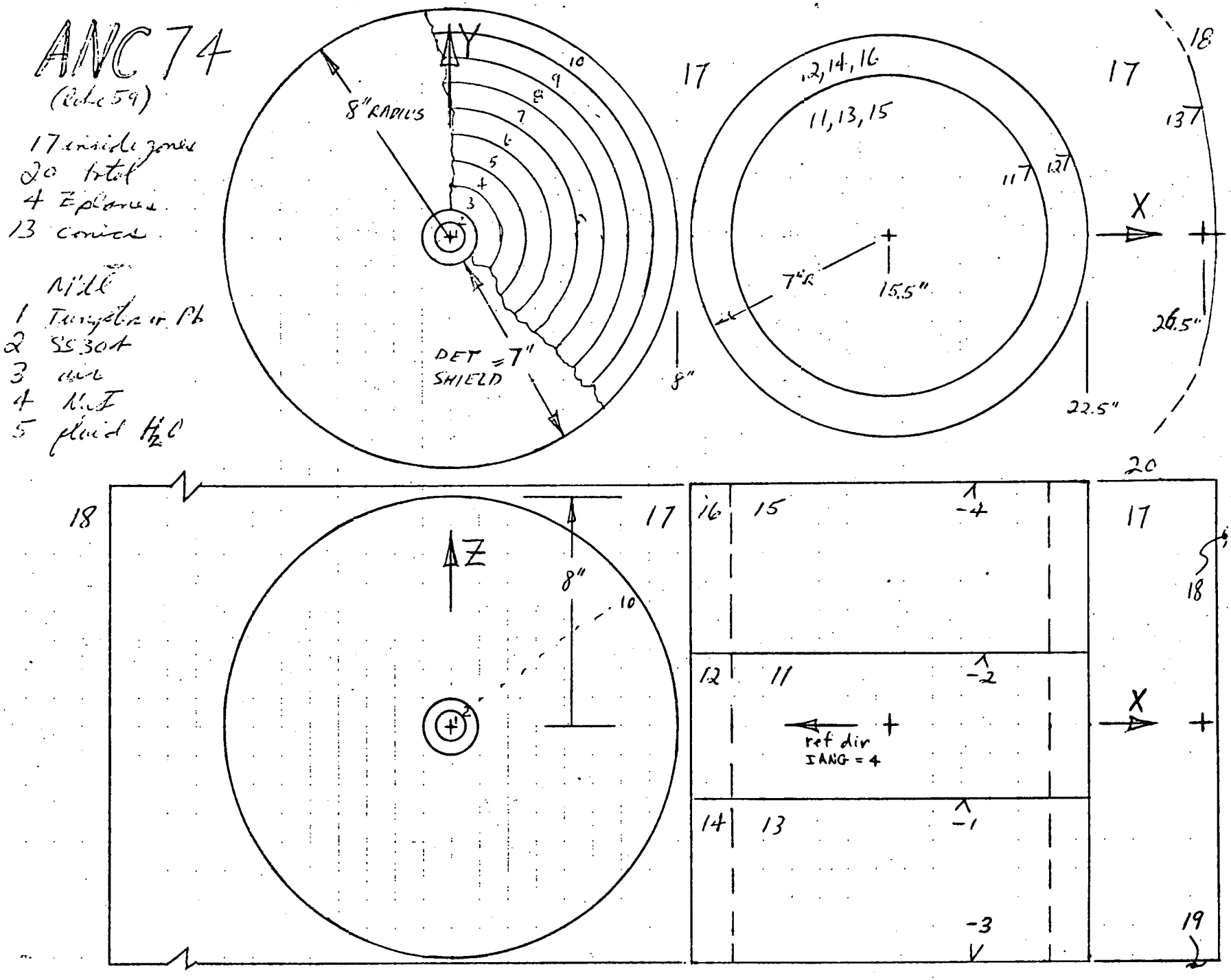

Figure 9. Spherical shell densitometer model geometry.

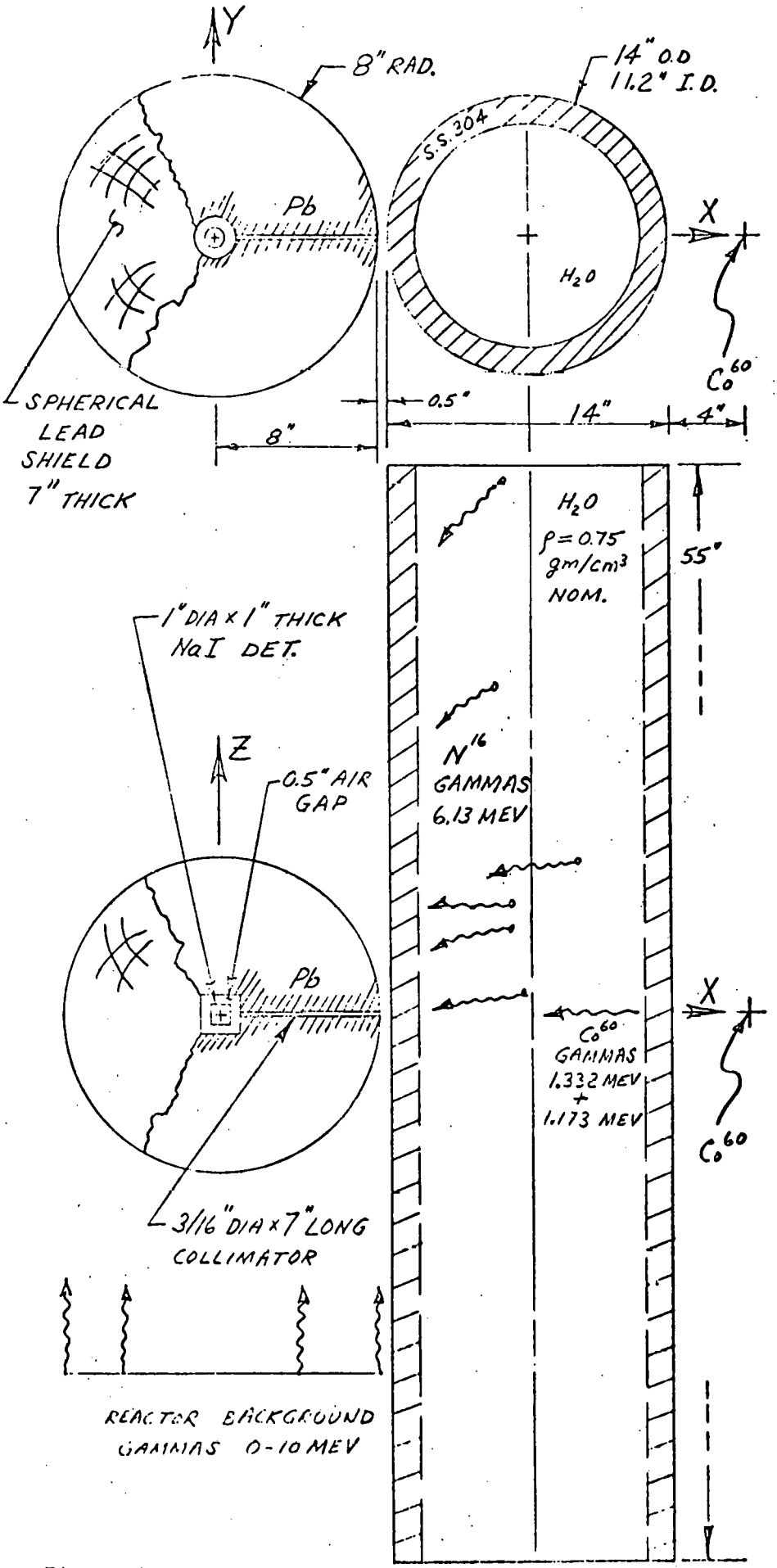

Figure 10. Final effective model geometry and sources.

Prototype Design Results and Performance

Various spectral simulations were calculated as shown in Figures 11-26 with a parameter index table for these spectra given in Table 2. Figure 11 shows an almost negligible photopeak at 6130 keV from the N^{16}; the N^{16} first and second escape peaks show up larger at 5619 keV and 5108 keV. There is no calibration (Co^{60}) source for Figures 11 and 12. Figure 12 is an expanded portion of Figure 11 and clearly shows the peak at 511 keV which is from positron annihilation photons generated in the large lead detector shield. It is important to note the smooth spectral shape from 600 to 2000 keV; this allows one to readily perform background subtraction using extrapolation. Since there is some uncertainty as to the shape of the spectrum from the reactor background, two shapes were used. The first case is the skew shape of Figure 2 (page 5) and the other is a flat shape or uniform intensity per energy bin from 0.5 - 10 MeV; this latter case represents a "worst case" and will be emphasized in the discussion. When, for example, a 50 Ci Co^{60} source is added to the problem, the spectrum of Figure 12 is changed to that of Figure 16. In Figure 16, the Co^{60} peaks at 1332 and 1173 keV are clearly evident, as is the Compton edge peak at 900 keV. By extrapolating the continuum from 1500 to 3500 keV down to the region of 1050 to 1450 keV, this calculated background may be used for background subtraction to determine the net area under the photopeaks that is caused by the Co^{60} and represents a useful density signal. Although the background continuum caused by the N^{16} and reactor background leakage is not desirable, it does have a smooth enough shape and enough counts in it to allow adequate background subtraction. The only other alternative is even more massive high-Z shielding. The relative importance of this leakage contribution to the detector is illustrated in Table 3 (page 38). The distinction should be made between photons entering the detector (Table 3) and

TABLE 2

Figure Index for Various Spectral Simulations using a 1 X 1 NaI Detector, 7 inches of Lead Shielding, 3/16 inch Collimator, Water at 0.75 gm/cc, and the Sources of Table 1 in the Geometry of Figure 10.

Figure No. → / Co^{60} Strength, Curies →		Sample Time 5 seconds			Sample Time 1 Second	
		Graph Range, MeV			Graph Range, MeV	
		0 -10	0 - 2		0 -10	0 - 2
Reactor Background Flat	0	11	12		-	-
	10	13	14		23	24
	50	15	16		-	-
Reactor Background Skew	0	17	18		-	-
	10	19	20		25	26
	50	21	22		-	-

Figure 11.

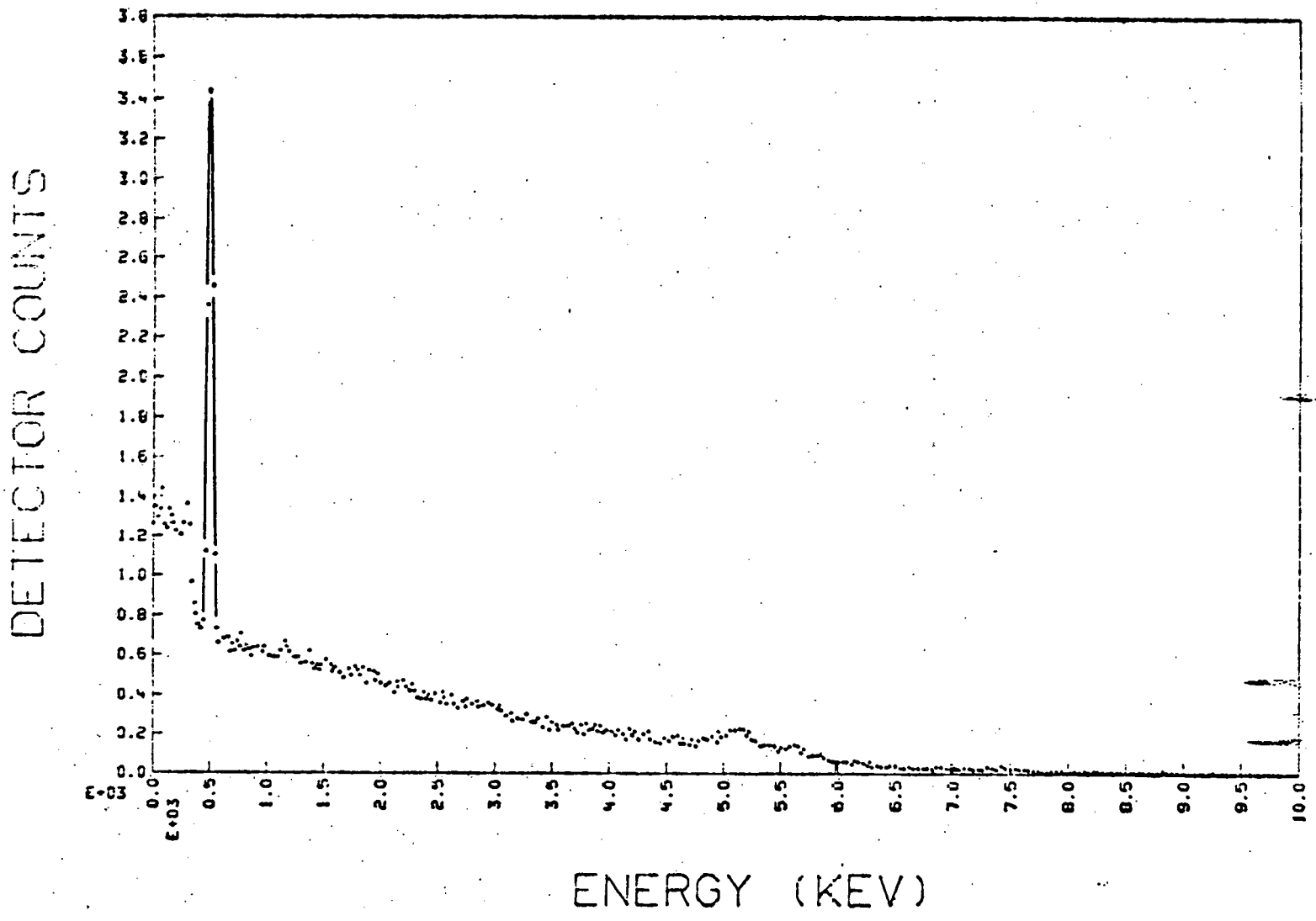

36 NAI1X1 7 PB 3/16 COLL 5SEC OCI FLAT
130644 CTS,KEV 0. 10000.0
EV/CH=20000.0 CTS FRACTION= 2.592E-01

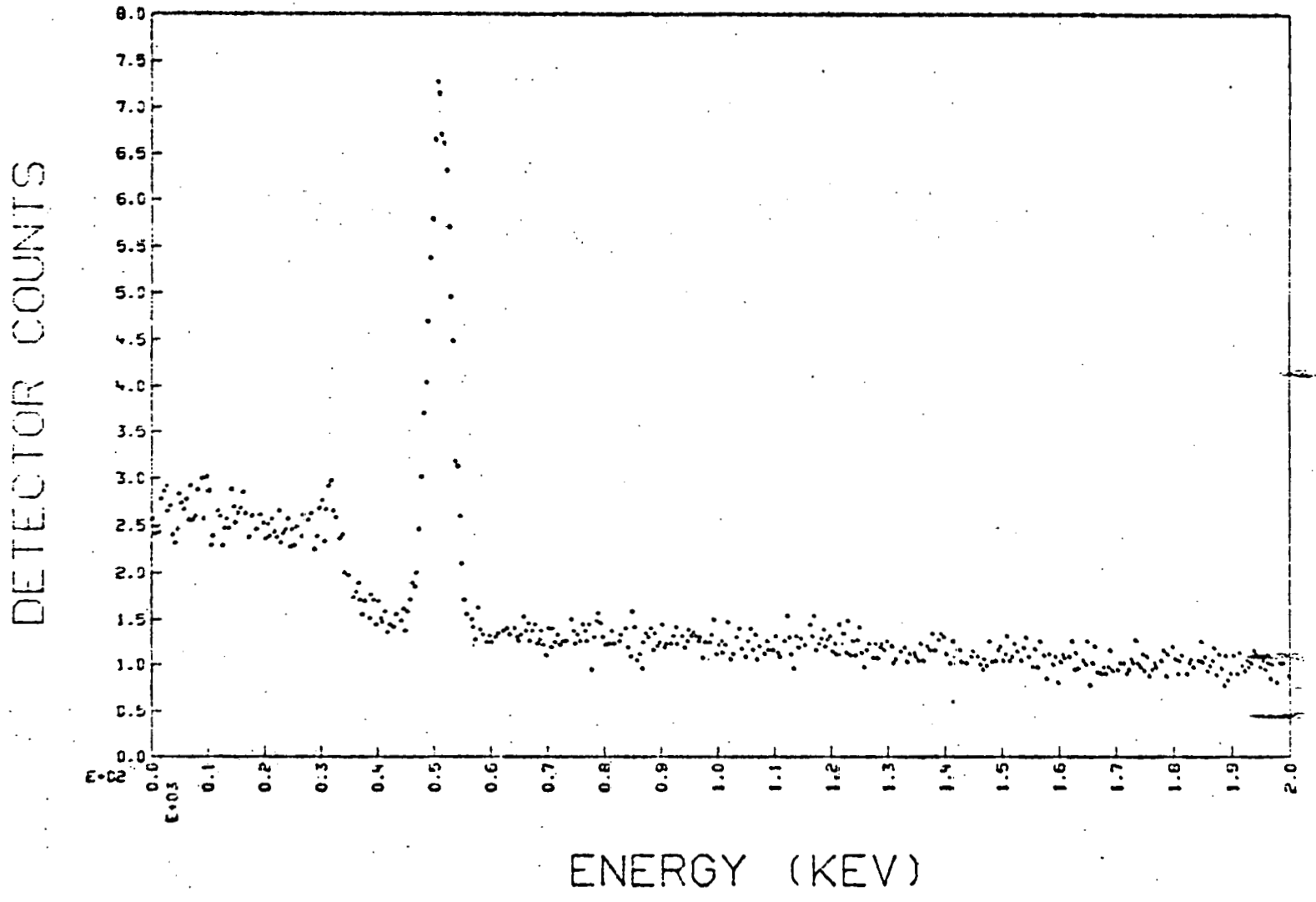

Figure 12.

36 NAI1X1 7 PB 3/16 COLL 5SEC OCI FLAT
130644 CTS,KEV 0. 10000.0
EV/CH= 4000.0 CTS FRACTION= 2.592E-01

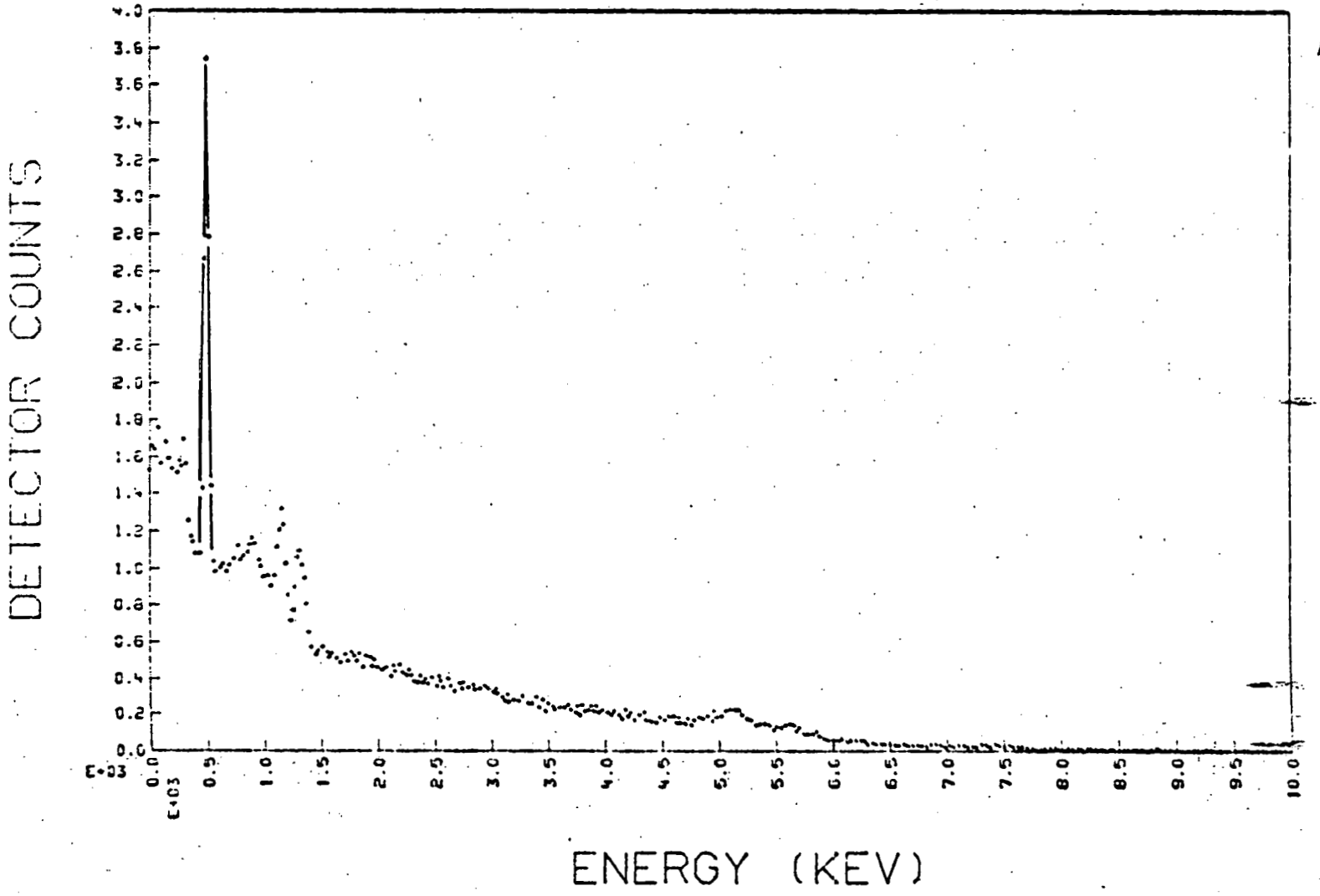

Figure 13.

38 NAI1X1 7 PB 3/16 COLL 5SEC 10CI FLAT
156218 CTS,KEV 0. 10000.0
EV/CH=20000.0 CTS FRACTION= 2.729E-01

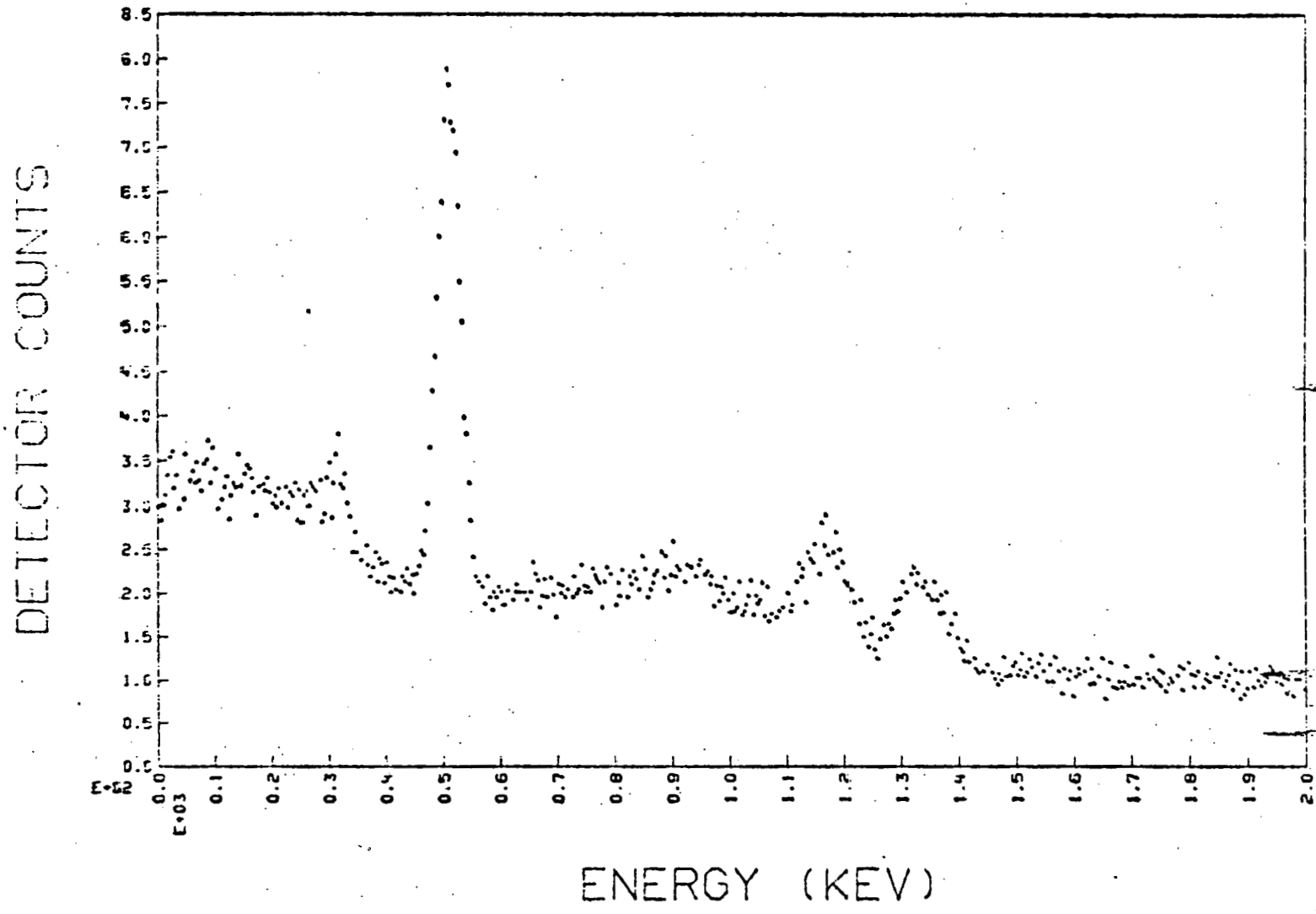

Figure 14.

38 NAI1X1 7 PB 3/16 COLL 5SEC 10CI FLAT
156218 CTS,KEV 0. 10000.0
EV/CH= 4000.0 CTS FRACTION= 2.729E-01

Figure 15.

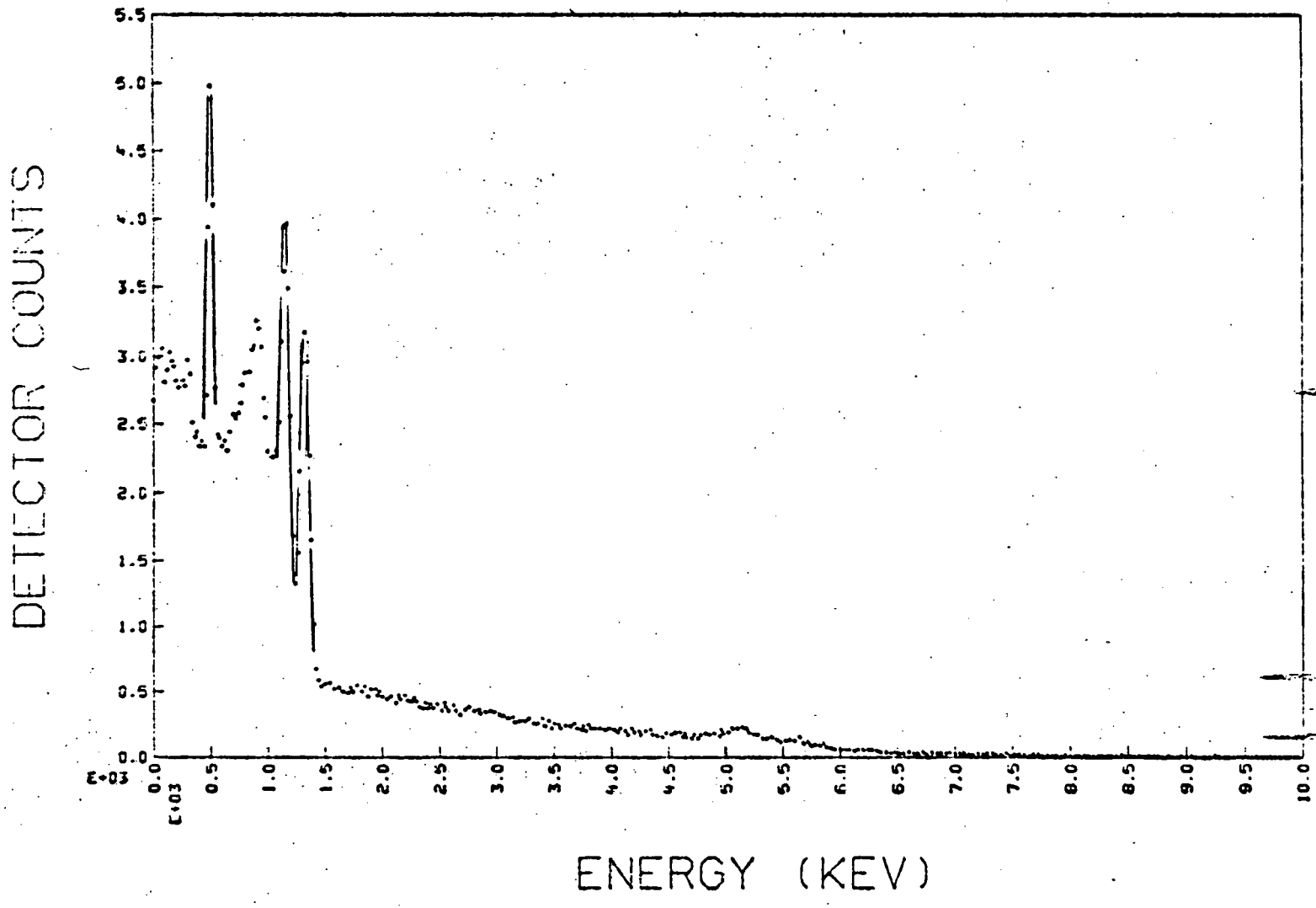

40 NAI1X1 7 PB 3/16 COLL 5SEC 50CI FLAT
258967 CTS,KEV 0. 10000.0
EV/CH=20000.0 CTS FRACTION= 3.063E-01

Figure 16.

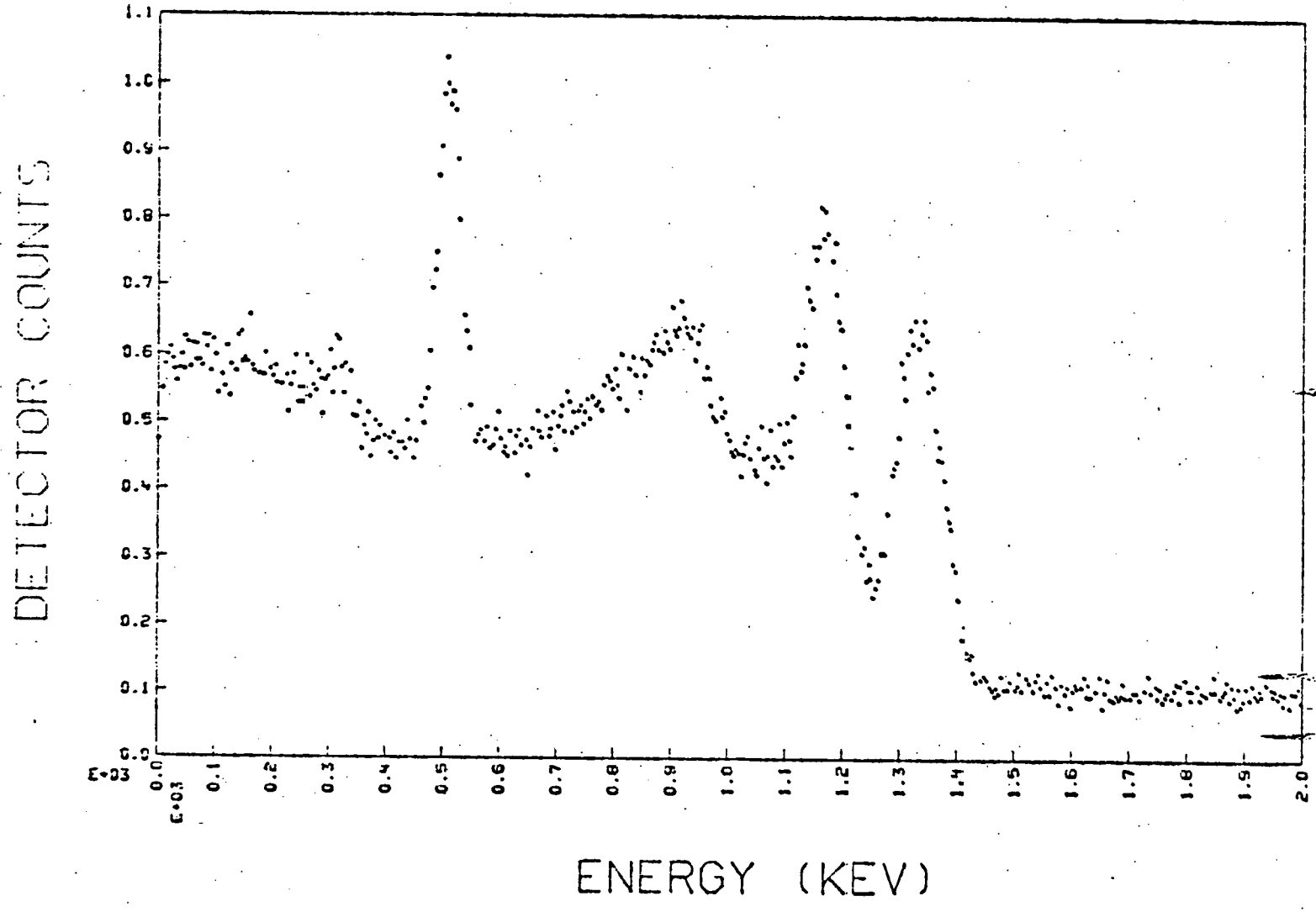

40 NA11X1 7 PB 3/16 COLL 5SEC 50CI FLAT
258967 CTS,KEV 0. 10000.0
EV/CH= 4000.0 CTS FRACTION= 3.063E-01

Figure 17.

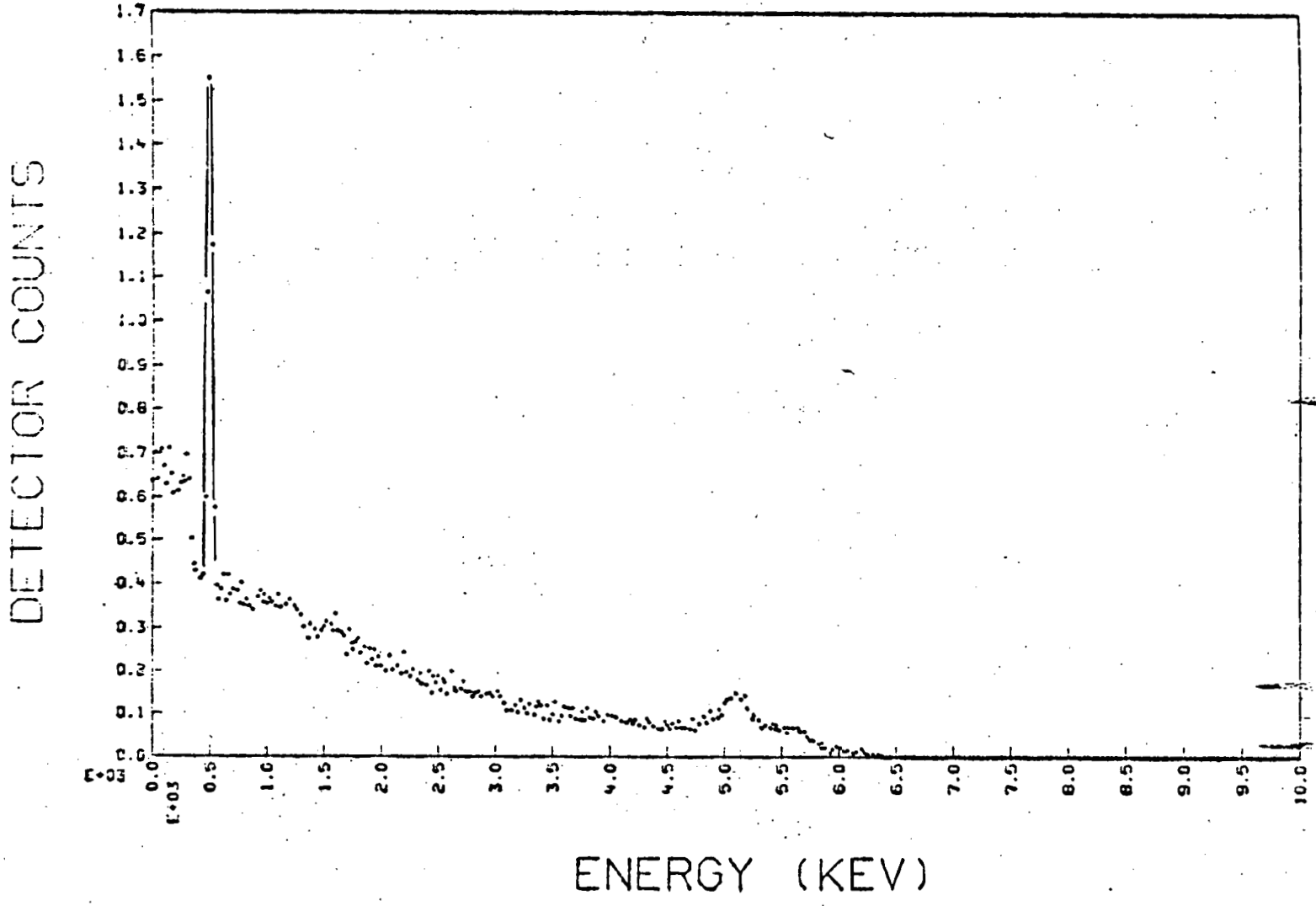

37 NA11X1 7 PB 3/16 COLL 5SEC 0C1 SKEW
63855 CTS,KEV 0. 10000.0
EV/CH=20000.0 CTS FRACTION= 2.632E-01

Figure 18.

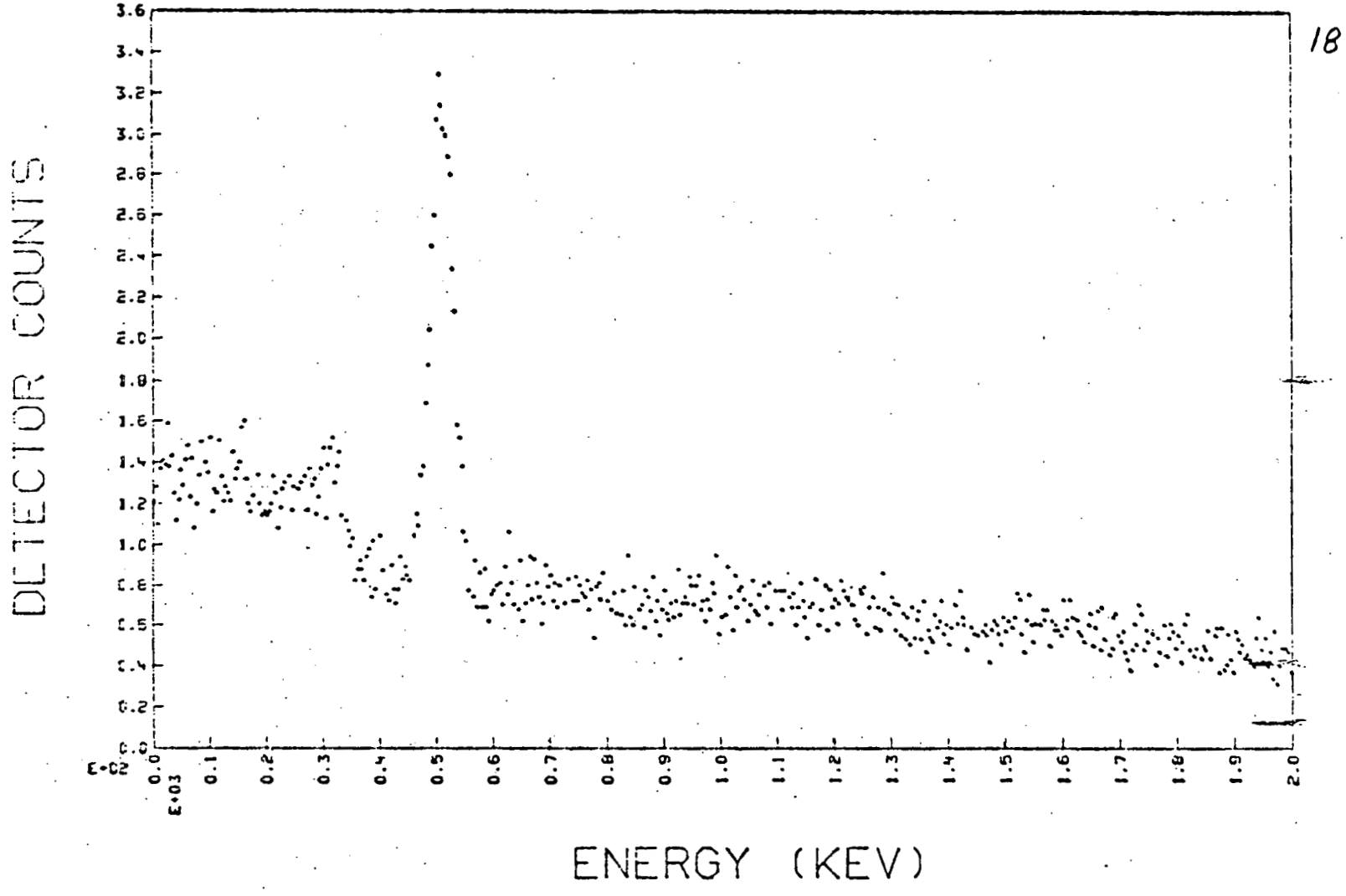

37 NAI1X1 7 PB 3/16 COLL 5SEC OCI SKEW
63855 CTS,KEV 0. 10000.0
EV/CH= 4000.0 CTS FRACTION= 2.632E-01

Figure 19.

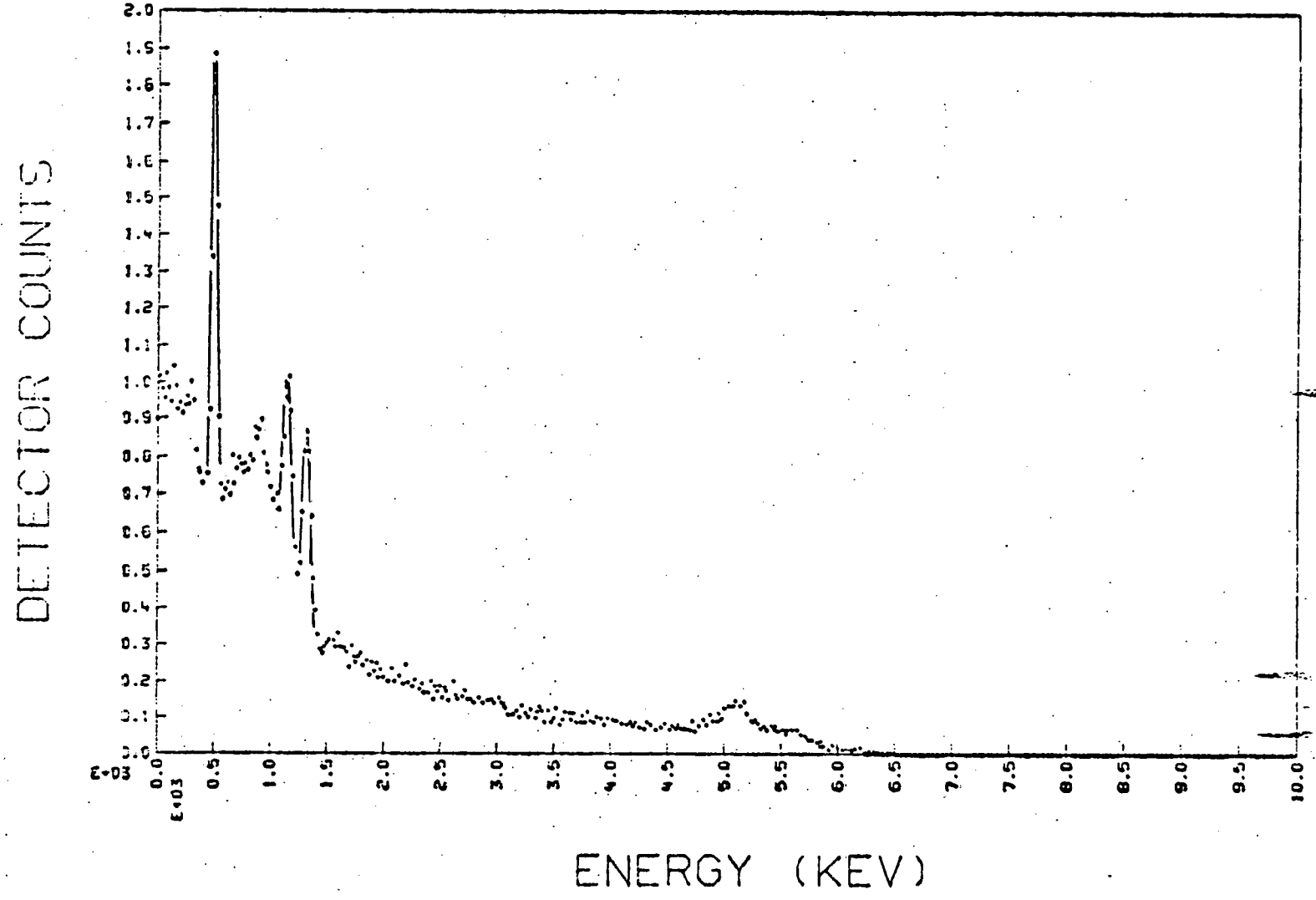

39 NAI1X1 7 PB 3/16 COLL 5SEC 10CI SKEW

89429 CTS,KEV 0. 10000.0

EV/CH=20000.0 CTS FRACTION= 2.877E-01

Figure 20.

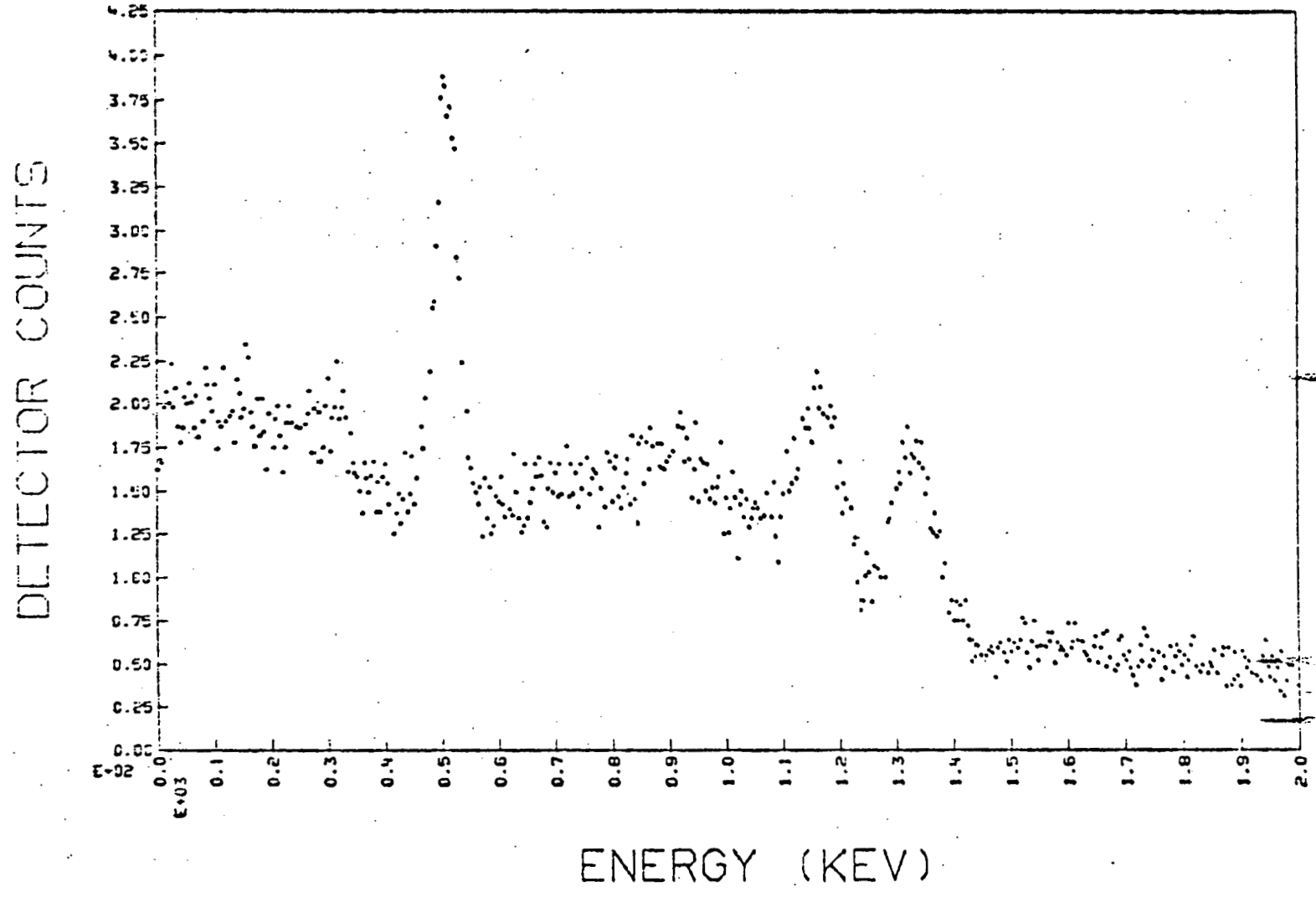

39 NAI1X1 7 PB 3/16 COLL 5SEC 10CI SKEW
89429 CTS,KEV 0. 10000.0
EV/CH= 4000.0 CTS FRACTION= 2.877E-01

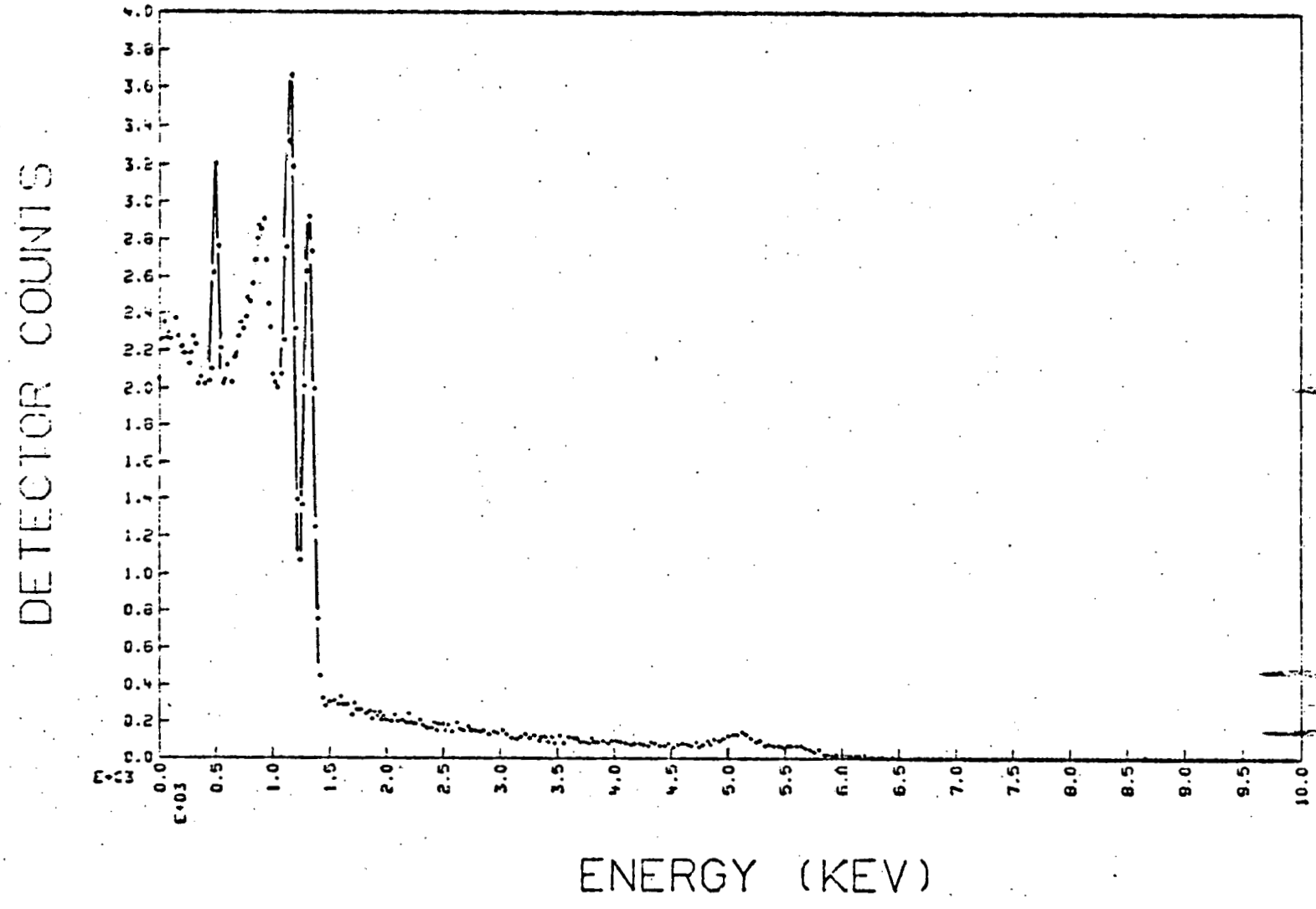
DETECTOR COUNTS
E+03
ENERGY (KEV)
41 NAI1X1 7 PB 3/16 COLL 5SEC 50CI SKEW
192178 CTS,KEV 0. 10000.0
EV/CH=20000.0 CTS FRACTION= 3.292E-01

Figure 21.

21

Figure 22.

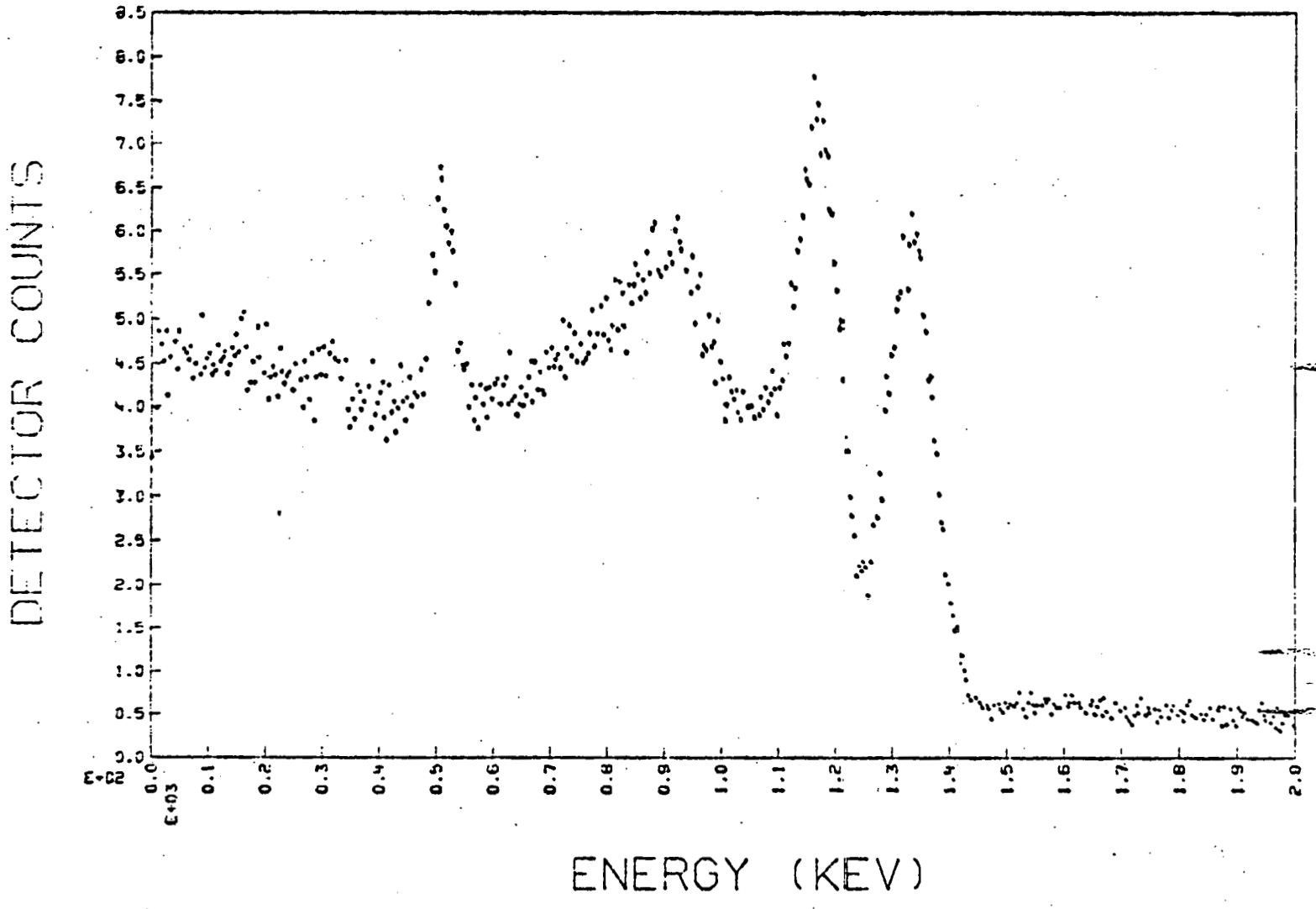

41 NAI1X1 7 PB 3/16 COLL 5SEC 50CI SKEW
192178 CTS,KEV 0. 10000.0
EV/CH= 4000.0 CTS FRACTION= 3.292E-01

Figure 23.

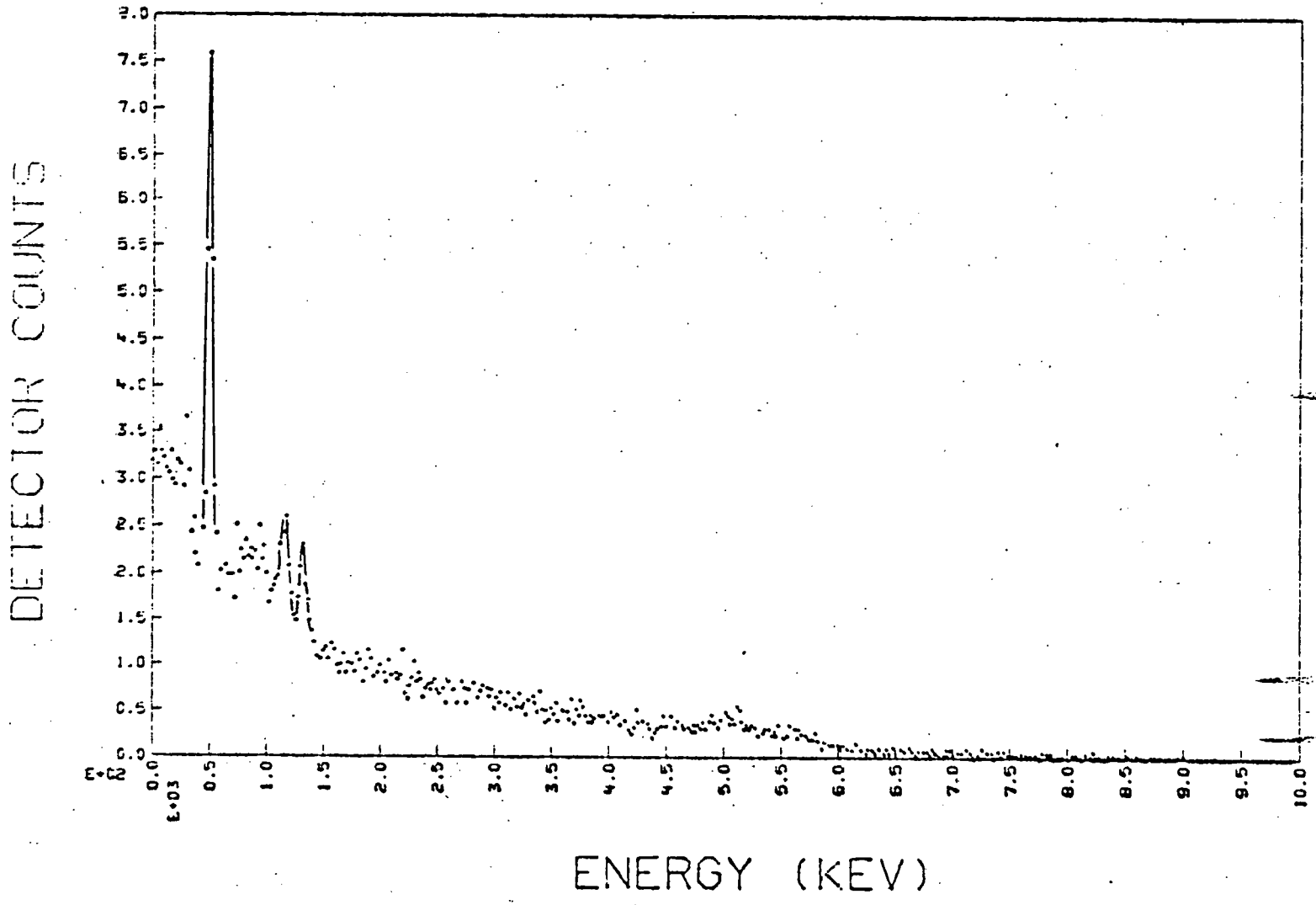

34 NA1 1X1 7 PB 3/16 COLL 1SEC 10CI FLAT
31212 CTS,KEV 0. 10000.0
EV/CH=20000.0 CTS FRACTION= 2.727E-01

Figure 24.

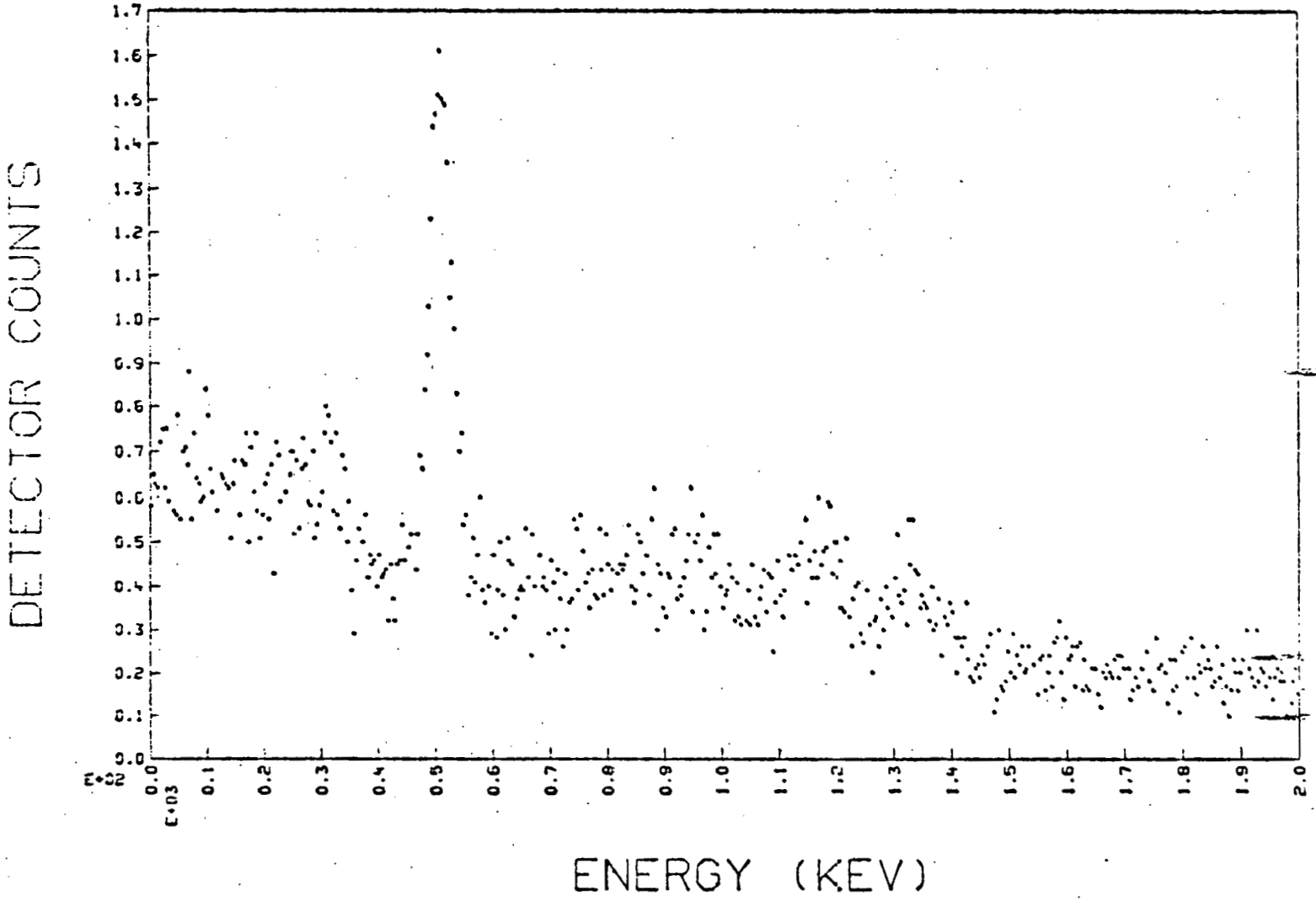

34 NAI1X1 7 PB 3/16 COLL 1SEC 10CI FLAT
31212 CTS,KEV 0. 10000.0
EV/CH= 4000.0 CTS FRACTION= 2.727E-01

Figure 25.

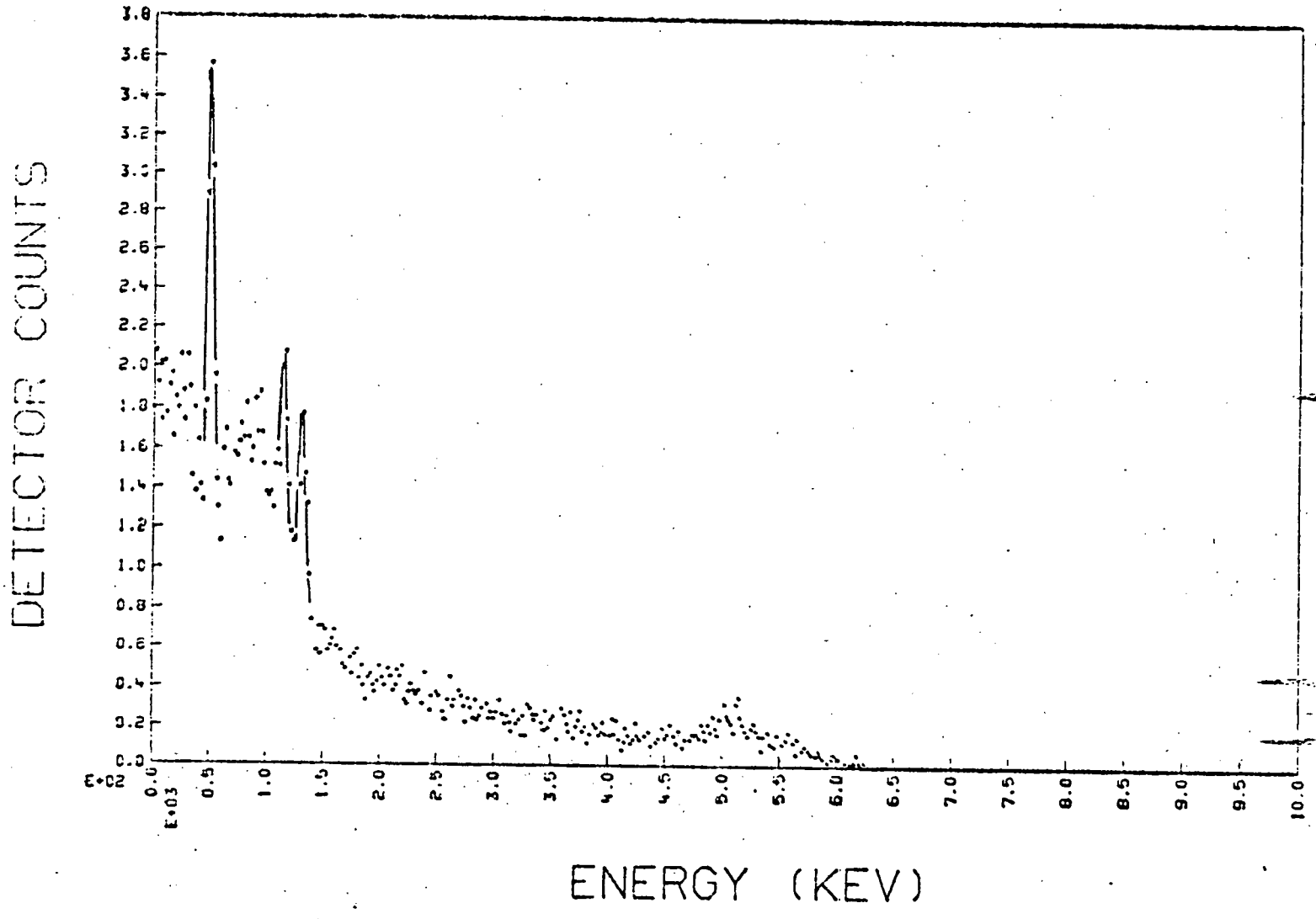

35 NAI1X1 7 PB 3/16 COLL 1SEC 10CI SKEW
17843 CTS,KEV 0. 10000.0
EV/CH=20000.0 CTS FRACTION= 2.870E-01

Figure 26.

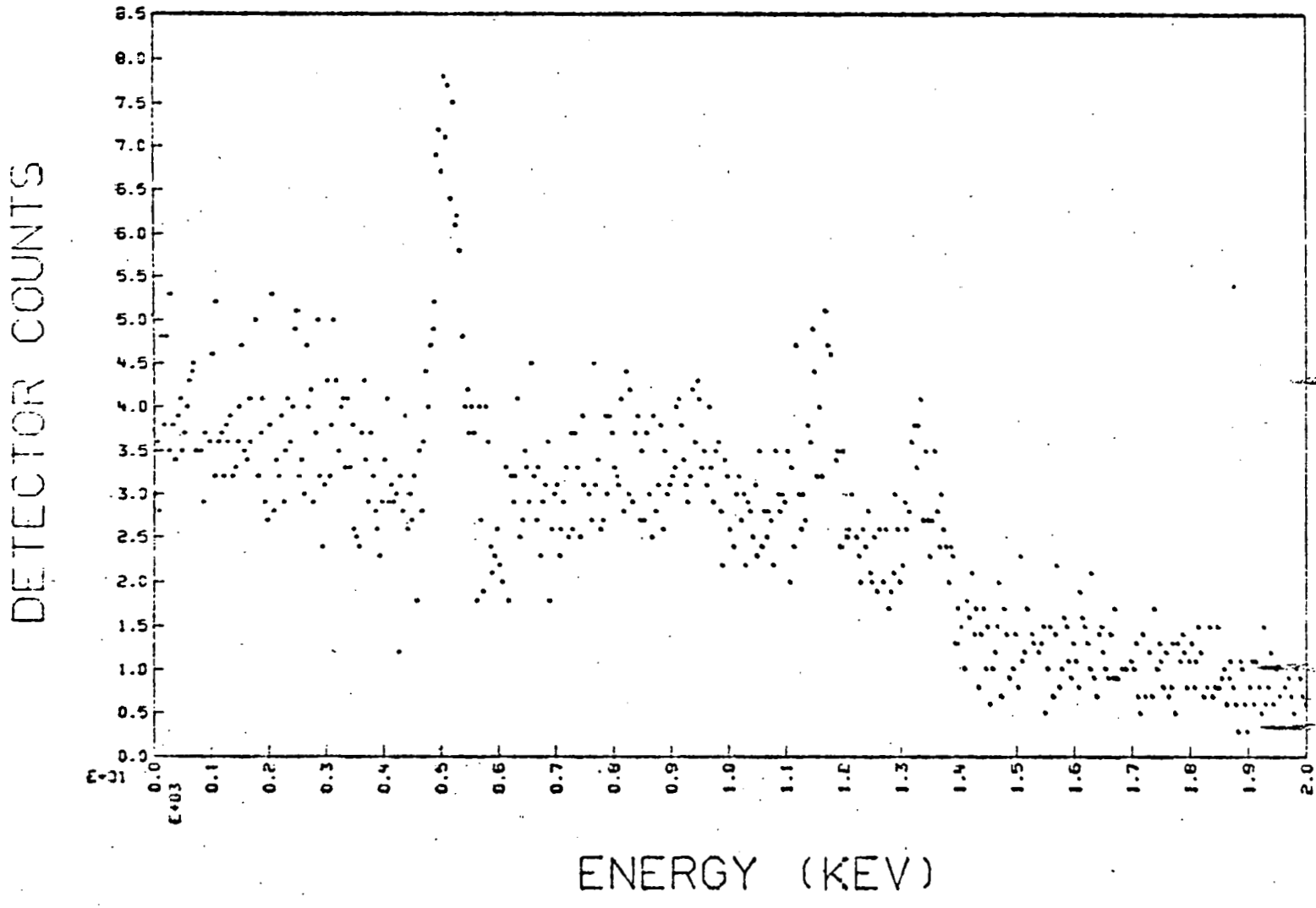

35 NAI1X1 7 PB 3/16 COLL 1SEC 10CI SKEW
17843 CTS,KEV 0. 10000.0
EV/CH= 4000.0 CTS FRACTION= 2.870E-01

TABLE 3

Source Contributions Entering the Detector

Source Origin		Photons/sec Entering Detector (Flat Reactor Background)		Photons/sec Entering Detector (Skew Reactor Background)	
N^{16} shielding leakage					
continuum		28 800		28 800	
6.13 MeV		5 940	21.9%	5 940	31.7%
511 keV		2 270		2 270	
N^{16} direct	6.13 MeV	810	0.5%	810	0.7%
down collimator					
50 Ci Co^{60} direct	1173 keV	31 050		31 050	
down collimator	1332 keV	37 200	40.4%	37 200	58.4%
Reactor Background					
continuum		58 000		10 000	
511 keV		5 000	37.2%	700	9.2%
		169 070	100%	116 770	100%

photons absorbed or counted by the detector (Figures 11-26).

To give quantitative meaning to the spectral information of Figures 11-26, one may integrate relevant portions of the spectrum and divide the resulting detector counts by the sample time to obtain a detector count rate for a given energy window. This has been done with the results tabulated in Table 4. In Table 4, the first row is the total photon input rate to the detector; the second row is the total detector count rate and the third row is the total detection efficiency obtained by dividing the second row by the first. The fourth and fifth rows are count rates of energy windows (FWTM = full width at 1/10 maximum = 1.826 X FWHM) centered on the Co^{60} peaks at 1173 and 1332 keV. Rows six to nine are from arbitrary, uniform energy windows on the smooth spectral continuum just above the signal windows. The total background strength is indicated in columns 36 and 37 (0 Ci of Co^{60}) and may be used to subtract from the other columns to obtain the net signals from the Co^{60} sources. The lower (1094 - 1252 keV) signal window has more net signal counts than the upper window because it derives its signal from the 1173 keV photopeak and also from the upper portion of the Compton continuum from the 1332 keV photons. This entire net signal is valid and usable and in practice both signal windows should be used to derive a total net signal that is indicative of the water absorption.

Using the weaker, upper signal window only, a simplified signal-to-noise analysis will now be given using data in Table 4. There are two obvious ways one could implement background subtraction in practice. First, one could leave the Co^{60} source on all the time and measure the spectrum above the signal window well enough to extrapolate the background to be subtracted from the signal window. This would probably require several upper energy windows and

TABLE 4

NaI 1 X 1, 7" Pb, 3/16" Dia. Coll., 0.75 gm/cm^3 H_2O

137 μCi/cm^3 N^{16}, Co^{60} 4" Away from Pipe

Count Rate, cps in integration region, keV / SPECTRUM RUN NO.	FLAT 0 Ci 5 sec 36	SKEW 0 Ci 5 sec 37	FLAT 10 Ci 5 sec 38	SKEW 10 Ci 5 sec 39	FLAT 50 Ci 5 sec 40	SKEW 50 Ci 5 sec 41	FLAT 10 Ci 1 sec 42	SKEW 10 Ci 1 sec 43
1. $\int$ DET INPUT	100 820	48 520	114 470	62 170	169 070	116 770	114 470	62 170
2. $\int$ 0 - 10 000	26 129	12 771	31 244	17 886	51 793	38 436	31 212	17 843
3. η_D (%)	25.92	26.32	27.29	28.77	30.63	32.92	27.27	28.70
4. $\int$ 1094 - 1252	999	569	1 710	1 274	4 530	4 077	1 707	1 280
5. $\int$ 1246 - 1419	1 009	554	1 556	1 110	3 734	3 291	1 513	1 075
6. $\int$ 1500 - 2000$^-$	2 582	1 345	2 582	1 345	2 582	1 345	2 552	1 314
7. $\int$ 2000 - 2500$^-$	2 110	976	2 110	976	2 110	976	2 127	1 002
8. $\int$ 2500 - 3000$^-$	1 795	775	1 795	775	1 795	775	1 788	765
9. $\int$ 3000 - 3500$^-$	1 416	574	1 416	574	1 416	574	1 420	598

an estimate of the general background shape that has been experimentally predetermined. This method has the advantage that the background information is derived for the same sample time and flow conditions that prevail for the signal window information. This method is a little more difficult to implement than the second obvious method but it should yield better results. The second obvious method uses a chopped Co^{60} source. In this method, the background to be used for subtraction is measured in the signal window during the off-time of the Co^{60} source, but synchronization of the sampling and chopper must be maintained. For simplicity, the second method will be used to illustrate the signal-to-noise ratio calculation. The specific example of a 10 Ci Co^{60} source with a skew reactor background is illustrated in Table 5. If the other data in Table 4 is used in a manner similar to that in Table 5, then Figure 27 may be constructed. Figure 27 plots the signal-to-noise ratio versus sampling time for various conditions. The 25 Ci source curves were obtained by scaling the 10 Ci and 50 Ci data. The noise in Figure 27 is simply the standard deviation and the curves in Figure 27 are shown dashed for very short sample times because very poor statistics renders the definition of noise used meaningless. Again, it must be emphasized that these calculations are for the weaker, upper peak signal only; the lower peak signal has a signal about 27% stronger. Thus, the signal-to-noise ratio that could be achieved from the system is better than is indicated in Figure 27. From Figure 27, one can see that the shape of the reactor background source, skew or flat, soft or hard, becomes less relevant for increasing Co^{60} source strengths. For any reasonable number of detector counts, the signal-to-noise ratio increases with the square root of the sampling time. The question of what signal-to-noise ratio is adequate depends on the range of water density encountered and how the signal and the noise depend on water density.

TABLE 5

An example of a simplified signal-to-noise ratio calculation for a 10 Ci Co^{60} source with a skew reactor background.

1) Assume a sample time of 0.2 seconds, i.e., 0.2 seconds for measuring S + B = signal + background and 0.2 seconds for measuring B only, for a total measuring time of 0.4 seconds.

2) Use $\dot{S} + \dot{B}$ = 1110 cps col 39, row 5, Table 4

Use $\dot{B}$ = 554 cps col 37, row 5, Table 4

3) S + B = 1110 X 0.2 = 222 cts $\quad \sigma_1 = \sqrt{S + B} = 14.90$

B = 554 X 0.2 = 111 cts $\quad \sigma_2 = \sqrt{B} = 10.54$

S = 111 cts $\quad \sigma_T = \sqrt{\sigma_1^2 + \sigma_2^2} = 18.25$

4) $S/\sigma_T = 6.10$, using only the 1332 keV photopeak window.

$$S/\sigma_T = \sqrt{\frac{(\dot{S} + \dot{B}) - (\dot{B})}{(\dot{S} + \dot{B}) + \dot{B}}} \times \sqrt{t}$$

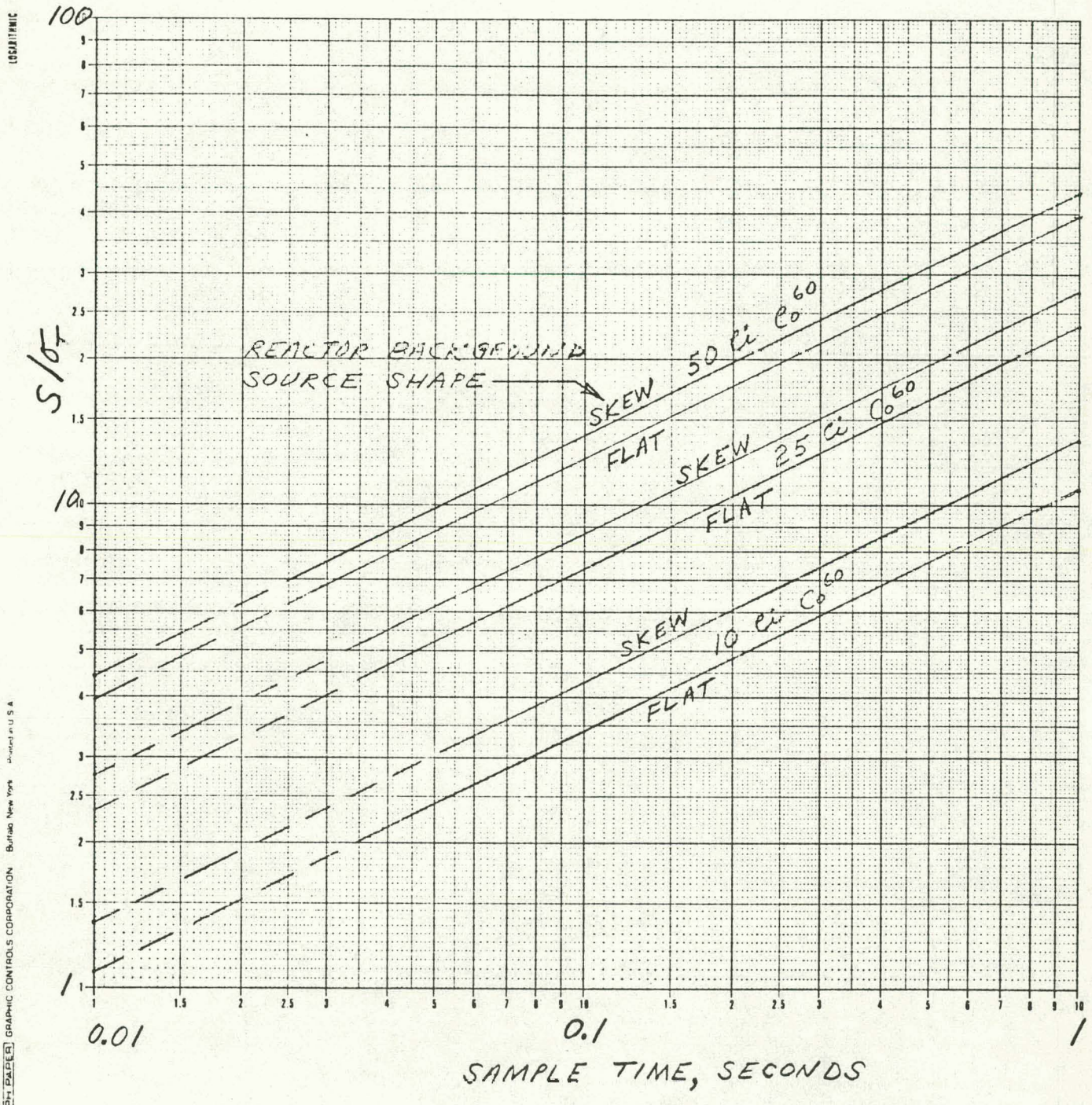

Figure 27. Signal-to-noise ratio versus sampling time using only the 1332 keV peak of Co^{60}.

Scaling from the Prototype Design

Using the geometry of Figure 10 (page 19), the upper Co^{60} peak signal entering the collimated detector as a function of water density has been calculated and the reuslts are shown in Figure 28. The results have been normalized to the water density of 0.75 gm/cm^3 because all previous data has used this nominal value. The slope of the line in Figure 28 simply yields the absorption coefficient for water at that energy. The signal in Figure 28 is directly proportional to the detector signal in the signal-to-noise ratio calculations. The background dependence on water density is more complicated; the N^{16}-to-reactor background ratio may vary from 0.59 to 3.45 depending upon whether the reactor background is flat or skewed as was shown in Table 3 (page 38). Consider the case of the skew reactor background and a 50 Ci Co^{60} source, if the N^{16} contribution is assumed to be proportional to the water density, 78% of the background will be reduced to zero as the water density approaches zero. Since most of the noise at the nominal operating point of ρ = 0.75 gm/cm^3 comes from the spectral background, a dramatic improvement in signal-to-noise ratio should result as the water density decreases.

One may scale collimator diameter changes upon the prototype design and performance. Consider the case of the 50 Ci Co^{60} source and the skew reactor background when changing the collimator from 3/16 to 4/16 inch, and using a sampling time of 0.2 seconds. The current value of S/σ_T = 19.8 is read from Figure 27. Since the new collimator diameter is still a fraction of the detector diameter, the photopeak efficiency at 1332 keV may be assumed constant (it will decrease slightly, see Figure 3). The down-collimator contribution of N^{16} is a negligible 0.7% (see Table 3). The down-collimator contribution of the Co^{60} should increase with the solid angle which is a factor of $(4/3)^2$ = 1.78. If the net Co^{60} signals in Table 4, column 41 were increased by 1.78, then the new value of S/σ_T = 28.2. Thus S/σ_T could be improved by 42% by increasing

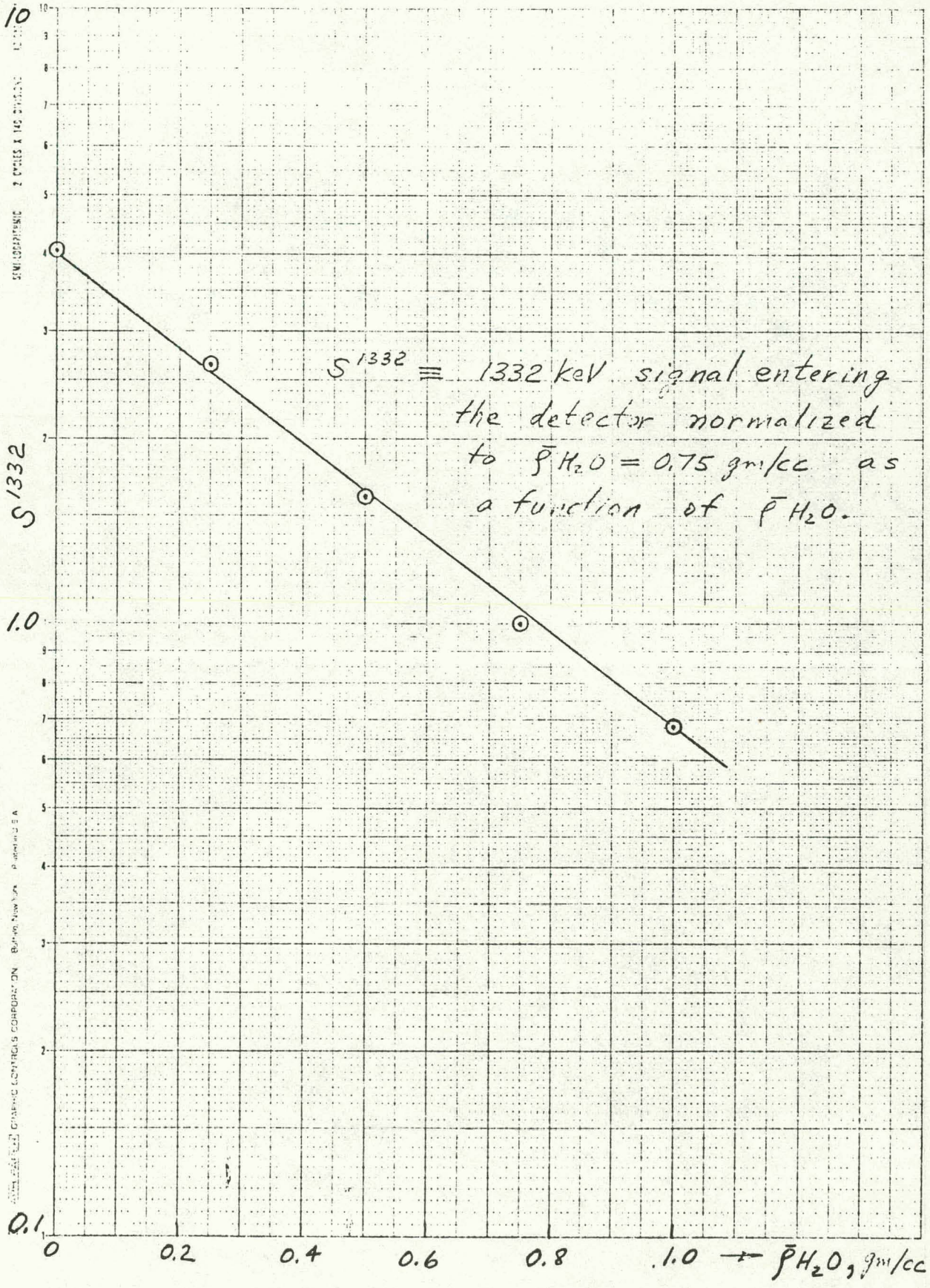

Figure 28. Relative strength of the 1332 keV signal of Co^{60} transmitted through the pipe as a function of water density.

the collimator diameter from 3/16 to 4/16 inch. The price one pays is a higher detector count rate; the old total detector count rate was 38,436 cps and the new value would be approximately 58,600 cps. This new value is not excessive but it is for a value of water density of 0.75 gm/cm^3. The increased count rate may reduce the dynamic range of water density that may be measured before saturation (detector electronics deadtime) effects take place at low water densities. Some of the deadtime effects may be unfolded depending upon the nature of their source in the detector and electronics.

Source strength effects upon signal-to-noise ratio may easily be scaled from the prototype design data in Table 4, as has been demonstrated with the 25 Ci curves of Figure 27. The net signal (S + B column - B column) is simply scaled directly to the source strength to calculate a new S + B value for use in the signal-to-noise calculation.

Source position changes may be similarly scaled using the $1/r^2$ dependence. The present r value (source-to-detector distance) is 26 inches. The 50 Ci source 4 inches away from the pipe will be equivalent to a 66.57 Ci source 8 inches away from the pipe.

Detector size effects may also be scaled using the efficiency data in Figure 3 and the source data in Table 3, making the assumption that uncollimated sources will also scale with detector cross-sectional area. One can easily estimate that shielding a 2 X 2 detector will be far more difficult than shielding a 1 X 1.

Prototype Calculational Detail and Additional Calculations

Of the sources listed in Table 3 (page 38), the first, which is the N^{16} shielding leakage was the most difficult to calculate for several reasons. This is a

high energy, distributed volume source of high intensity. For these reasons, its contribution over a significant length of the coolant pipe nearest the detector must be considered. For computational purposes, the 55-inch length of pipe from which N^{16} radiation was modeled was divided into 5 inch long cylindrical segments. The middle segment was bisected by the densitometer axis (X-axis of Figure 10, page 19). To compute the photon flux entering the detector more accurately, a spherical shell detector shield and spherical detector were used. This was necessary because a successful shield transmits a very small fraction of the incident photons and longer computer runs are required to obtain good statistics on the transmitted fraction. To help alleviate this problem, a computational technique using photon multipliers (in the spherical shield) and weighting factors was employed. Two identical comparative runs with and without photon multipliers were made with identical results except for the much higher precision using the multiplier technique. The angular emission from the N^{16} was further confined within a cone aimed toward the detector from the center of the source segment. The nominal value of the cone's semi-apex angle, α, was 45°. The real photons that are emitted outside of this conical distribution constitute 85% of all emissions but they cannot make a significant contribution to the flux entering the detector and should not be followed computationally. This may be understood by considering the energy of the scattered Compton photon as shown in Figure 29. A source photon originally inclined 45° away from the detector must scatter through 90° to turn towards the detector. A Compton photon scattered through 90° or 180° must have an energy less than $m_o c^2$ (= 511 keV) or $m_o c^2/2$, respectively. For a 6.13 MeV source photon, using Figure 29, the 90° scattered photon has an energy of 470 keV and the 180° scattered photon has an energy of 245 keV. Photons of these energies will have little chance of penetrating the shielding

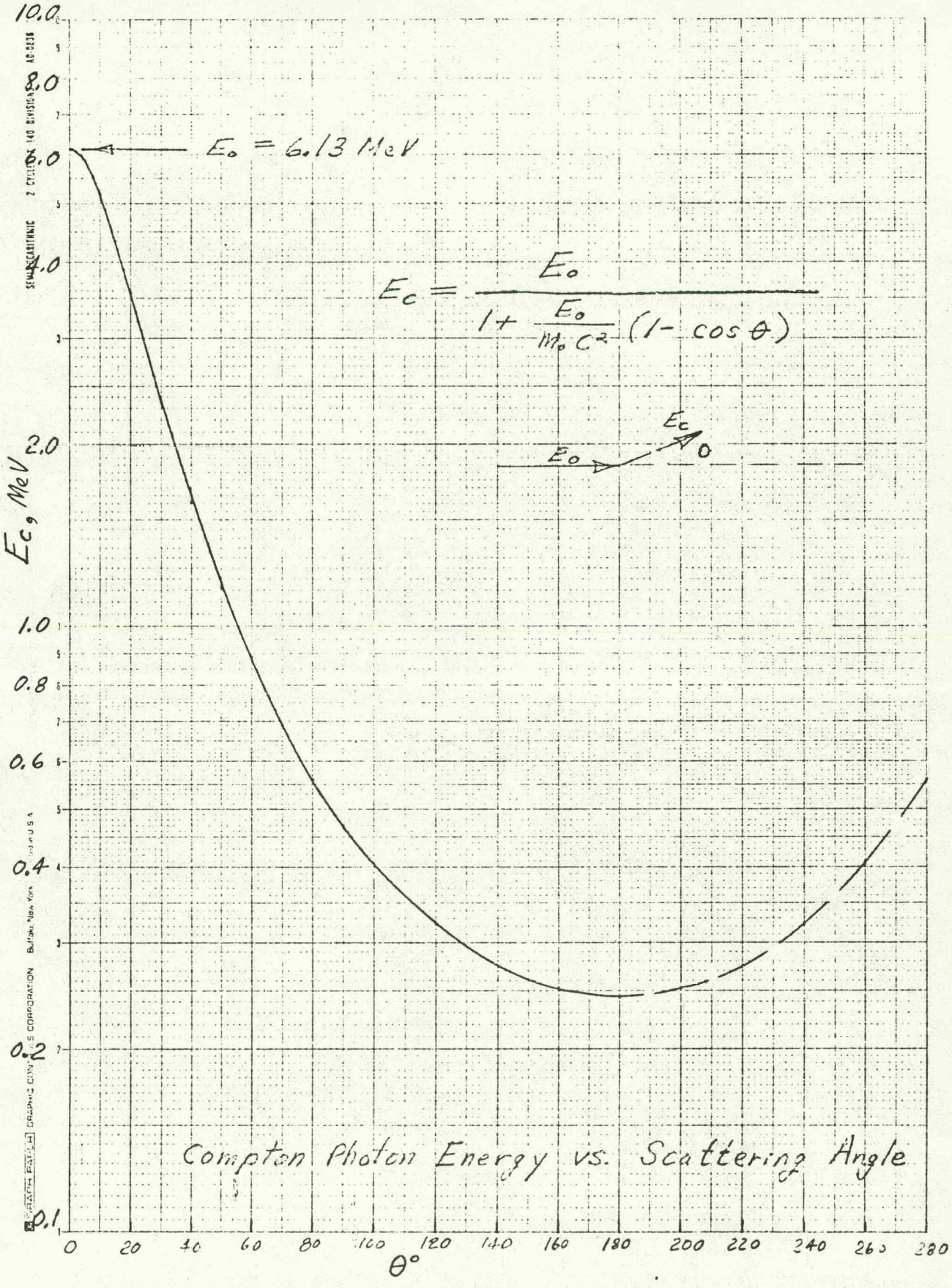

Figure 29. Compton photon energy as a function of scattering angle for an incident 6.13 MeV photon.

and adding to the detector signal. Even five successive 18 scattering events in the same plane in the same direction still results in a total scattering angle of 90 but with a low 1.56 MeV residual photon energy; this situation also has a very low probability of occurring. This explanation has been computationally verified by computer runs where the source cone apex angle was the parameter.

The total flux, F_1^T (photons per source photon), entering the detector from the different pipe segments is shown in Figure 30. The contribution falls off faster than $1/r^2$, as might be expected since the coolant pipe appears thicker at oblique angle transmission. The integrated contributions from the eleven 5-inch thick N^{16} disk sources of Figure 30 is shown in Figure 31. In Figure 31, the conical source solid angle factor has been included, and TF represents the true fractional transmission (photons per 4π-source photon) entering the detector.

The second strong source to the detector is the reactor background spectrum. Two different source spectral shapes were used here; a flat intensity profile was used as a worst case and a skew intensity profile shown in Figure 2 was used for the more likely situation. Parallel beam sources of this type were incident on the detector and shield assembly and the resulting fluxes entering the detector are shown in Figures 32 and 33. Figures 31 to 33 all represent the transmission through seven inches of lead. They all have a maximum which is higher in energy for the harder source spectrum; however, the energy maxima ranges only from 1.8 to 2.7 MeV for a very wide range in source hardness. It may help to understand this trend by considering the attenuation coefficient versus energy for lead shown in Figure 34. The attenuation coefficient is equivalent to the reciprocal of the mean free path and one can see that the mean

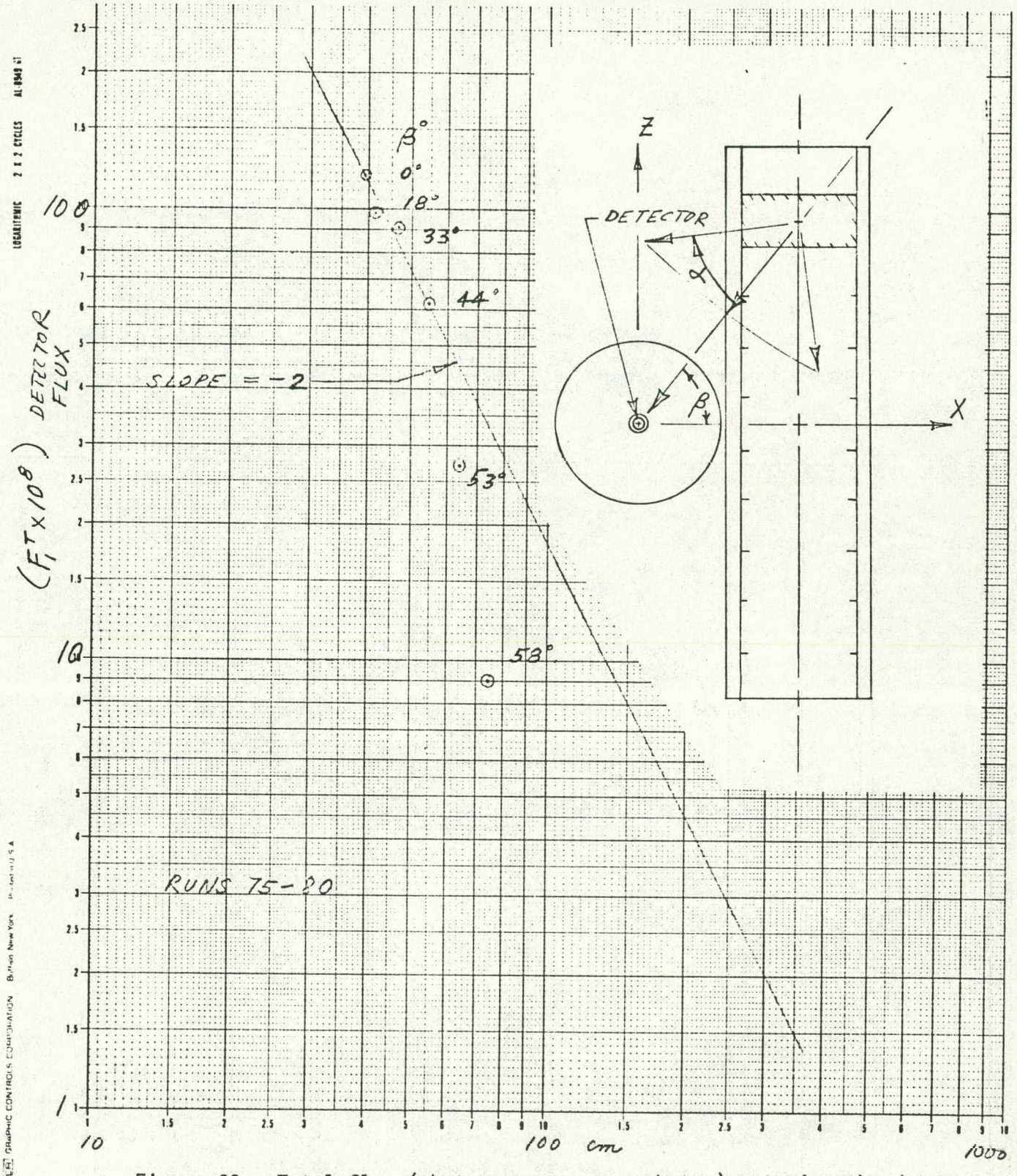

Figure 30. Total flux (photons per source photon) entering the detector from the N^{16} in the different pipe segments versus source - detector distance. Source semi-apex angle = α = 45°.

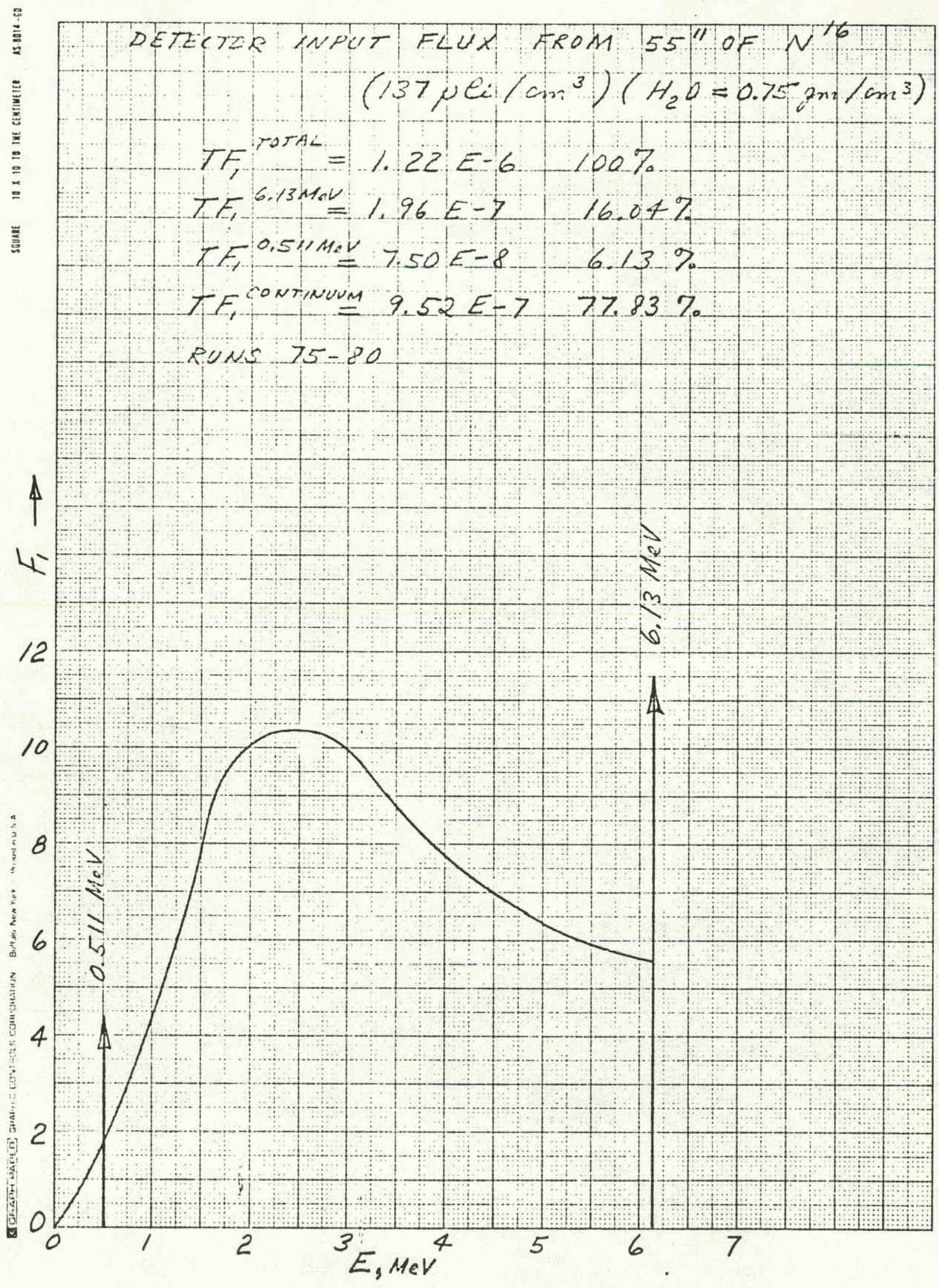

Figure 31. Detector input flux from N^{16}.

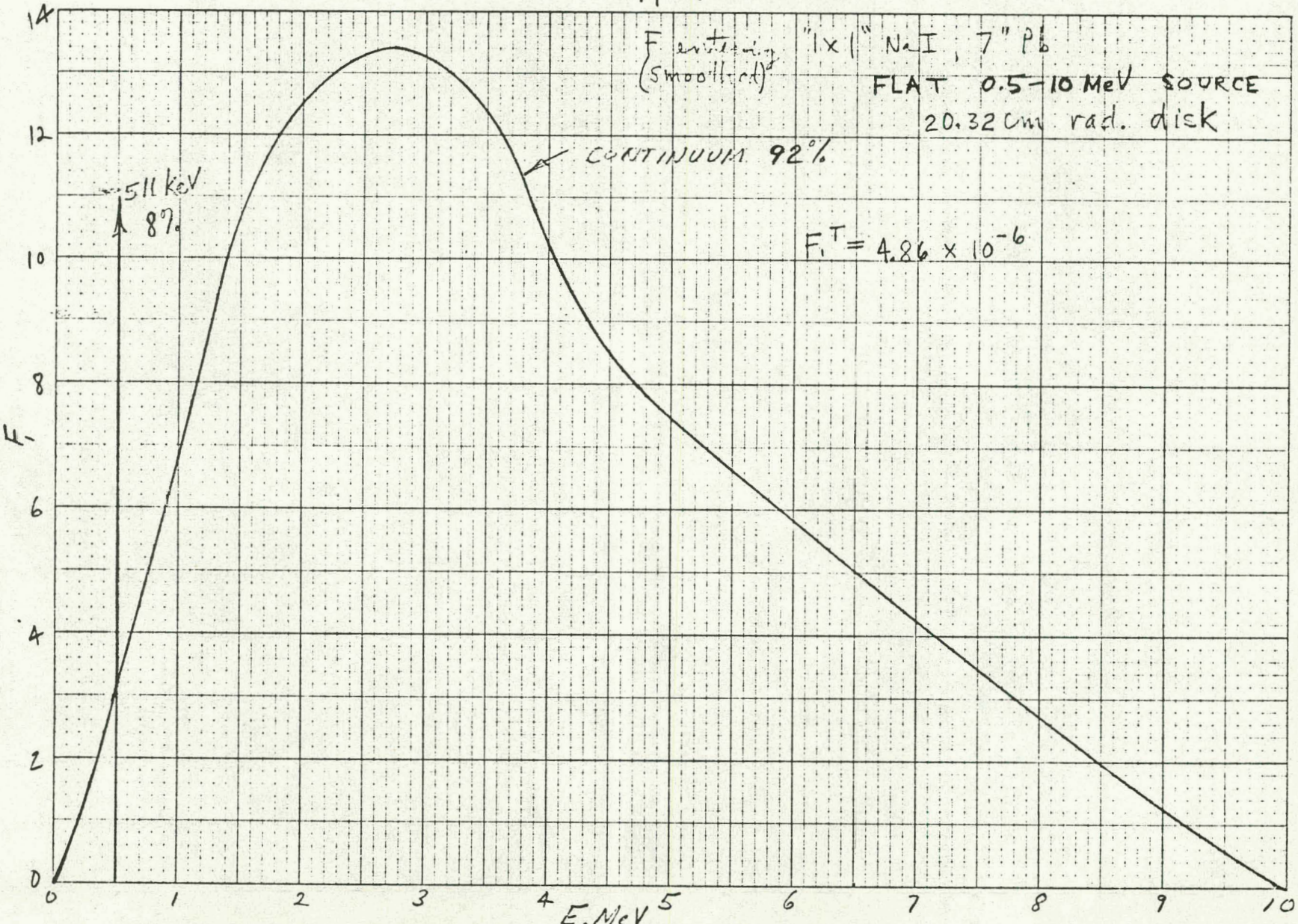

Figure 32. Detector input flux from flat reactor background source.

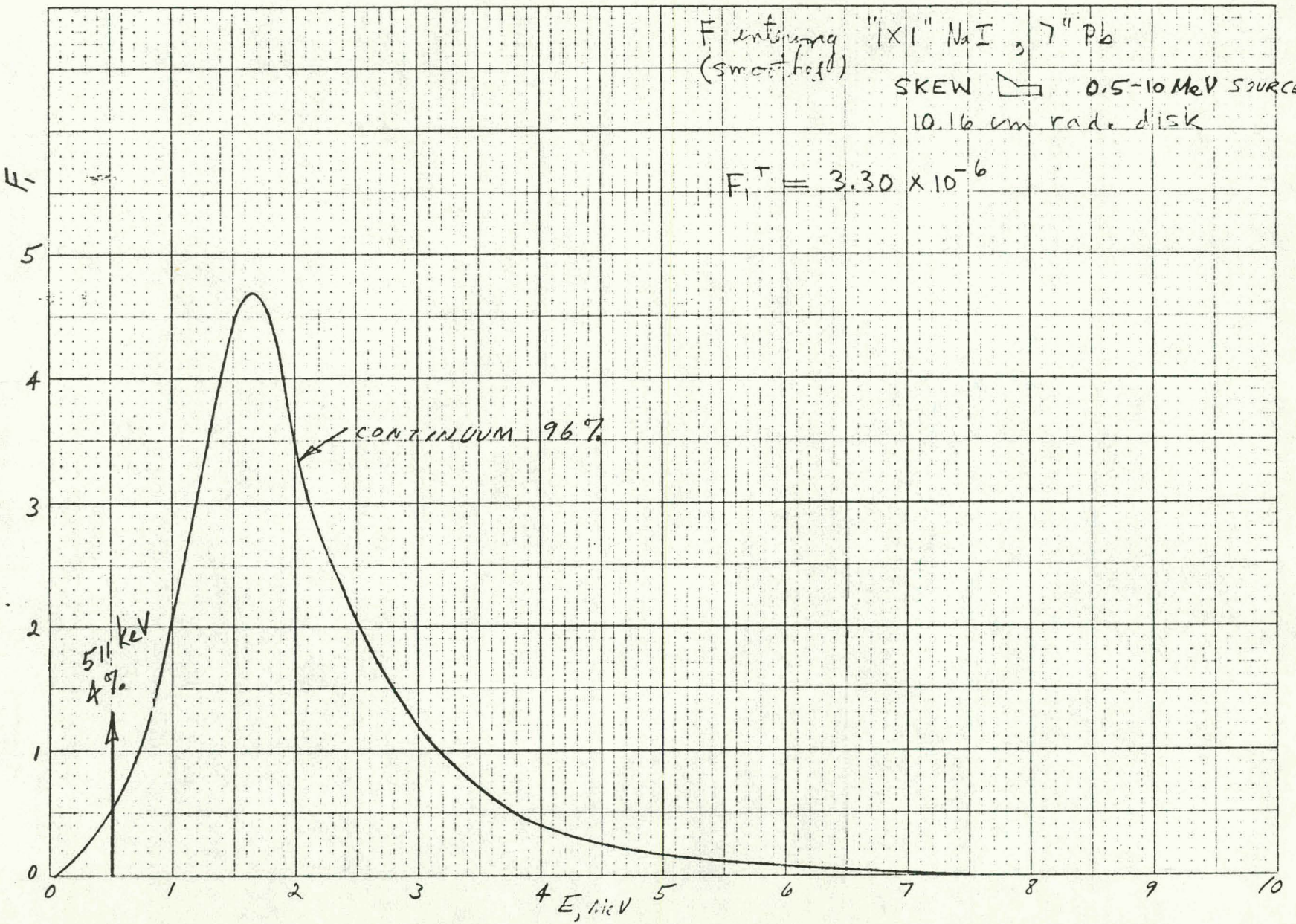

Figure 33. Detector input flux from skew reactor background source.

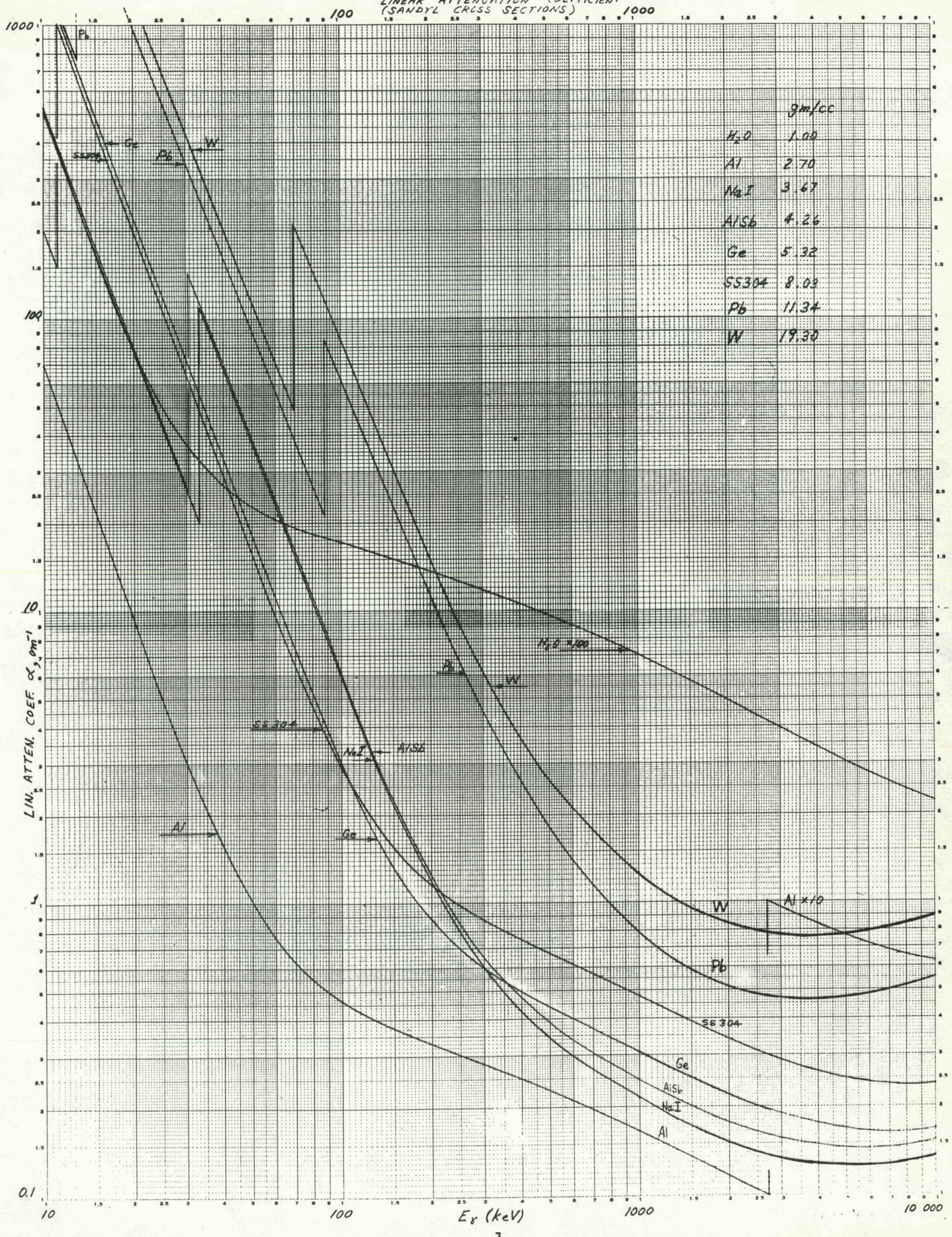

Figure 34. Attenuation coefficient (cm^{-1}) or the reciprocal of the mean free path for photons in various materials.

free path goes through a maximum for lead at 3.6 MeV. Above this energy, pair production soon dominates and the subsequent positron annihilation nearest the detector in the lead creates 511 keV photons that sometimes reach the detector; below this energy, especially below 1 MeV, the absorption in the lead becomes very high, thus very little low energy flux reaches the detector.

The contributions down the collimator path from inside-wall scatter and leakage that end up in the broad energy continuum are relatively small; most of the collimated radiation is at the source photopeak energy. For the N^{16} source, 88% of the collimated radiation is in the photopeak. For the Co^{60} source, 96% of the collimated radiation is in the photopeak. The continuum contributions from these sources are negligible and have been excluded from Table 3 and the spectral modeling.

Initial calculations started with a 2 x 2 detector and 4 inches of shielding rather than the final values of a 1 x 1 detector and 7 inches of shielding. The initial calculations were only partial because not all of the sources were calculated. The partial results indicated the trend to very high detector count rates and so complete calculations were not done. By scaling the partial results to the complete data for the 1 x 1 detector shielded with 7 inches of lead, the relative shielding effects for various detector sizes are summarized in Table 6. The consequences of inadequate shielding are dramatically emphasized in Table 6. The detector count rate from the N^{16} source alone for a 2 x 2 detector and 4 inches of lead shielding is 8.18×10^5 cps; if the reactor background were included, this could typically increase this count rate by a factor of two. The results shown in Table 6 indicate the need for very conservative shielding design.

Table 6

Detector Count Rate From 55" of N^{16} in the Pipe

Shielding	Spherical Detector Radius, cm	Equal Volume Cylindrical Detector Dia. x Ht., inches	Detector Entry Flux from Central 5" Segment of N^{16} in pipe	Detection Efficiency, %	Relative Detector Count Rate	Detector Count Rate from 55" of N^{16} in Pipe, Kcps
7" Pb	1.454	1 x 1	1.28×10^{-6}	26	1.00	37
7" Pb	2.540	1.75 x 1.75	3.40×10^{-6}	~41	4.17	154
4" W	2.908	2 x 2	9.08×10^{-6}	~46	12.55	464
4" Pb	2.908	2 x 2	1.60×10^{-4}	~46	221.0	818

Application Notes and Summary

The calculational models employed included a region around the detector of a 0.5 inch gap filled with air. This was intended to account for the practical need to isolate the detector crystal-photomultiplier assembly from thermal and acoustic shocks. In addition, the gain shifts significantly with temperature so that thermal isolation and stabilization will be required. A slow temperature drift could readily be compensated by using an AGC (automatic gain control) amplifier that "locks" on to a reference peak in the spectrum; this could include the upper Co^{60} peak or it could be provided by a stabilized light pulser. The photomultiplier should be optimized for high count rates; see "A High-Rate Phototube Base," by Cordon R. Kerns, to be published in IEEE Trans. Nucl. Sci., Feb. 1977.

The Co^{60} source should be contained in a shield container that has a remote controlled shutter. The shutter should be quite efficient because the spectral background shape must be accurately determined before the experiment. The Co^{60} source container could also be designed to remotely advance the source closer to the coolant pipe once the shutter has been opened. This would significantly improve the signal count rate.

The importance of accurate background subtraction cannot be overemphasized. Reducing the background by increasing the massive high-Z detector shielding beyond the amount used in this prototype design is strongly recommended where possible. For example, it would be desirable to replace the lead collimator region of the detector shield with a large tungsten cylindrical plug with the collimator hole in it. This would provide additional detector shielding from one of the strongest background sources--the volume of coolant water nearest the detector.

The use of multiple sources along different collimation paths incident on one detector is not recommended. The multiple source energy spectrum is very complicated with all the higher energy sources contributing Compton backgrounds in the region of the lower energy photopeaks. Spectral unfolding is difficult at best without the complications of a strong transient background. In addition, the spectrum one is trying to unfold is also a transient. Accurate spectrum unfolding requires a spectrum with very little statistical noise, i.e., long measurement times. This strongly conflicts with the predicted prototype performance data.

The complete densitometer designs discussed previously were designed to keep the detector count rate in the nominal range of 20,000 to 50,000 cps; this is for a water density of 0.75 gm/cm^3. As the water density goes to zero, the N^{16} signal goes away and the Co^{60} signals increase by factors of $\sim$4.1 and 4.5. If one considers a worst case, using the flat reactor background which is assumed to remain constant in time and a 50 Ci Co^{60} source, the detector count rate will go from 52,000 cps at a density of 0.75 gm/cm^3 to 125,000 cps at a density of zero. Of the 125,000 cps at zero density, 110,000 cps are from the Co^{60} source. If the detector and its electronics can handle this count rate, then the signal-to-noise ratio would be very high. Again using the upper energy Co^{60} peak only, the S/σ_T is estimated to be 97.8 for a 1 second sampling time or 43.7 for a 0.2 second sampling time at zero density. The noise is dominated by the statistics of the Co^{60} signal; the background contribution to the noise is negligible.

Neutron shielding must also be considered. The partial filling of the collimator with boron nitride, effectively shields the detector from thermal neutrons coming down the collimator. The rest of the detector could be

protected by boron nitride shielding built into the detector thermal and vibrational gap filler material. One might also coat the outside of the detector-photomultiplier assembly with a boron nitride loaded paste or epoxy. It may be desirable to coat the outside of the detector shield with cadmium. Cadmium neutron shielding should not be used adjacent to the detector because of activation gammas. Activation is not a problem with the boron shielding because the (n,α) reaction with B^{10} produces stable Li^{7} and an energetic (2.5 MeV) alpha particle. A very thin detector housing should stop the alpha particle without significantly attenuating the Co^{60} signal. Thermal neutrons incident on the NaI will activate the detector; the problem has been observed to be the production of I^{128}. I^{128} has a 25 minute half-life and several emissions: a beta emission up to 2.12 MeV (90+%) and 2 gammas 441 keV (14%) and 969 keV (0.3%) and a few others. For a thermal neutron flux of 10^{7} n/cm^{2}-sec incident on a 1 x 1 NaI detector, a rough estimate of the I^{128} creation rate is 1.1×10^{7} atoms I^{128}/sec. After a few half-lifes, the decay rate will equal the creation rate and a strong built in source could result.

The signal processing and data storage could be done in many ways. A system with some redundancy would seem desirable. One way this could be achieved would be to have seven or more single channel analyzers driving counters that are periodically read out and reset. At the same time the full pulse height spectrum, say using 256 channels, could be periodically dumped into a fast buffer for a few seconds before and after blowdown.

There appears to be no reason why one Co^{60} source could not be viewed by several separate detectors located on different points on a plane bisecting the pipe. This would only require designing the source case so that the source

could be seen by the several detectors. A source that advanced outside the case and up near to the pipe would be quite satisfactory. Of course, the practical necessity of supporting the considerable weight of the detector shields and the source shield needs to be addressed.

NOTICE

This report was prepared as an account of work sponsored by the United States Government. Neither the United States nor the United States Energy Research & Development Administration, nor any of their employees, nor any of their contractors, subcontractors, or their employees, makes any warranty, express or implied, or assumes any legal liability or responsibility for the accuracy, completeness or usefulness of any information, apparatus, product or process disclosed, or represents that its use would not infringe privately-owned rights.

NOTICE

Reference to a company or product name does not imply approval or recommendation of the product by the University of California or the U.S. Energy Research & Development Administration to the exclusion of others that may be suitable.

Printed in the United States of America
Available from
National Technical Information Service
U.S. Department of Commerce
5285 Port Royal Road
Springfield, VA 22161
Price: Printed Copy $; Microfiche $3.00

Page Range	Domestic Price	Page Range	Domestic Price
001–025	$ 3.50	326–350	10.00
026–050	4.00	351–375	10.50
051–075	4.50	376–400	10.75
076–100	5.00	401–425	11.00
101–125	5.50	426–450	11.75
126–150	6.00	451–475	12.00
151–175	6.75	476–500	12.50
176–200	7.50	501–525	12.75
201–225	7.75	526–550	13.00
226–250	8.00	551–575	13.50
251–275	9.00	576–600	13.75
276–300	9.25	601–up	*
301–325	9.75		

*Add $2.50 for each additional 100 page increment from 601 to 1,000 pages; add $4.50 for each additional 100 page increment over 1,000 pages.

Technical Information Department
LAWRENCE LIVERMORE LABORATORY
University of California | Livermore, California | 94550